

Article

Hydrogen Production through Bi-Reforming of Methane: Improving Ni Catalyst Performance via an Exsolution Approach

Ekaterina Matus ^{1,*}, Olga Sukhova ¹, Mikhail Kerzhentsev ¹, Ilyas Ismagilov ¹, Svetlana Yashnik ¹, Vladimir Ushakov ¹, Olga Stonkus ¹, Evgeny Gerasimov ¹, Andrey Nikitin ², Pankaj Bharali ³ and Zinifer Ismagilov ^{1,2}

¹ Boreskov Institute of Catalysis, SB RAS, 630090 Novosibirsk, Russia

² The Federal Research Center of Coal and Coal Chemistry, SB RAS, 650000 Kemerovo, Russia

³ Department of Chemical Sciences, Tezpur University, Napaam, Tezpur 784 028, Assam, India

* Correspondence: matus@catalysis.ru

Abstract: Hydrogen production through the bi-reforming of methane over exsolution-derived Ni catalysts has been studied. Nickel-based catalysts were prepared through the activation of (CeM)_{1-x}Ni_xO_y (M = Al, La, Mg) solid solutions in a reducing gaseous medium. Their performance and resistance to coking under the reaction conditions were controlled by regulating their textural, structural, morphological, and redox properties through adjustments to the composition of the oxide matrix (M/Ce = 0–4; x = 0.2–0.8; y = 1.0–2.0). The role of the M-dopant type in the genesis and properties of the catalysts was established. The efficiency of the catalysts in the bi-reforming of methane increased in the following series of M: M-free < La < Al < Mg, correlating with the structural behavior of the nickel active component and the anti-coking properties of the support matrix. The preferred M-type and M/Ce ratio determined the best performance of (CeM)_{1-x}Ni_xO_y catalysts. At 800 °C the optimum Ce_{0.6}Mg_{0.2}Ni_{0.2}O_{1.6} catalyst provided a stable H₂ yield of 90% at a high level of CO₂ and CH₄ conversions (>85%).

Keywords: hydrogen; methane; bi-reforming; Ni catalyst; dopant; exsolution



Citation: Matus, E.; Sukhova, O.; Kerzhentsev, M.; Ismagilov, I.; Yashnik, S.; Ushakov, V.; Stonkus, O.; Gerasimov, E.; Nikitin, A.; Bharali, P.; et al. Hydrogen Production through Bi-Reforming of Methane: Improving Ni Catalyst Performance via an Exsolution Approach. *Catalysts* **2022**, *12*, 1493. <https://doi.org/10.3390/catal12121493>

Academic Editors: Concetta Ruocco and Marco Martino

Received: 2 November 2022

Accepted: 19 November 2022

Published: 22 November 2022

Publisher's Note: MDPI stays neutral with regard to jurisdictional claims in published maps and institutional affiliations.

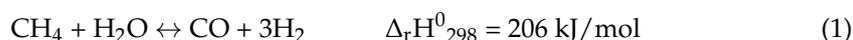


Copyright: © 2022 by the authors. Licensee MDPI, Basel, Switzerland. This article is an open access article distributed under the terms and conditions of the Creative Commons Attribution (CC BY) license (<https://creativecommons.org/licenses/by/4.0/>).

1. Introduction

Hydrogen is a versatile energy carrier and an important industrial raw material. About 75 million tons (Mt) of pure H₂ and 45 Mt of H₂ mixed with other gases are consumed annually [1]. The main consumer of pure hydrogen is the chemical sector (39 Mt), where H₂ is used in the production of ammonia, and oil refining (33 Mt), where it is needed for the hydrotreating and hydrocracking of oil [2]. Methanol synthesis and steel production are important sources of demand for hydrogen mixed with other gases. The large-scale use of hydrogen as an energy carrier requires the solution of various issues, including its efficient production, economical purification, safe storage, and transportation [3–5].

For H₂ production, conventional and renewable technologies are applied based on the use of fossil fuels (natural gas, heavy oils, naphtha, coal, etc.) and renewable resources (water, biomass, etc.), respectively [6–8]. At present, hydrogen is generally produced from natural gas (“gray hydrogen”) and coal (“brown hydrogen”), with small contributions from oil and electricity. “Gray hydrogen” is mainly manufactured through the steam reforming of methane (SRM, Reactions (1) and (2)), which is accomplished by CO₂ emission [9]:



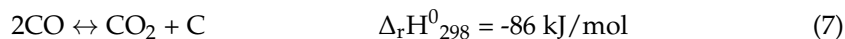
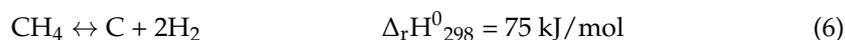
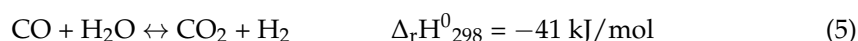
Today, H₂ production from fossil fuels emits about 900 Mt of CO₂ [10]. It is predicted that by 2050, the production of hydrogen from natural gas will be almost entirely based on low-carbon technologies: water electrolysis accounts for more than 60% of world

production, and natural gas in combination with CCUS (carbon capture, utilization, and storage) accounts for almost 40% (“blue hydrogen”) [10]. However, the future of the latter technology is doubtful [6,9,11], since greenhouse gas footprints from “blue hydrogen” are only 18–20% less than those from “gray hydrogen” due to the use of fossil C-derived energy to implement the CCUS technology. Thus, the improvement of cost-effective processes of converting methane into a hydrogen-containing gas is still relevant.

The combined steam and carbon dioxide reforming of methane (bi-reforming of methane, Reaction (3)) is an attractive way to catalytically generate hydrogen-containing gas from natural gas with CO₂ utilization [12–14]:



This is a unique environmentally and climate-friendly process that allows one to simultaneously utilize three greenhouse gases (carbon dioxide, methane, and water vapor). The obtained syngas can be used directly in certain processes, such as methanol production or the direct reduction of iron, or they can be used to produce pure hydrogen. In this case, concentrated CO streams can be captured and used in the production of formic acid, acetic acid, or functional copolymers [15–19]. The bi-reforming of methane is a complex process [20,21]. It involves the reactions of steam (1) and (2) and carbon dioxide (4) and the conversion of methane, leading to the production of the target products (synthesis gas or hydrogen), a number of additional reactions that increase the yield of hydrogen (5) and (6), and side reactions of carbon formation (6)–(9).



Extensive application in the reforming process was given to Ni-based catalysts due to their low cost, wide availability, and sufficiently high activity [22–28]. An obstacle that arises when using nickel catalysts is their deactivation under harsh reaction conditions and the impossibility of self-activation [29]. There are various strategies for improving the activity and stability of nickel catalysts: optimization of preparation mode [30,31] and support composition [32,33], application of different promoters (Mo, Pd, Pt, Rh, Re, or Mo) [34,35], variation of calcination and activation procedure [36–39]. For example, using La₂O₃ or MgO as basic support modifiers can prevent Ni agglomeration and promote CO₂ activation, which increases the activity and stability of the catalyst in the dry reforming of methane (DRM) [40,41].

Critical factors controlling catalyst performance and the rate of carbon deposits formation include the strength of metal–support interaction (MSI) and the nickel particle size. The Ni particle size significantly affects the carbon formation and removal reaction paths in DRM and, consequently, the amount and the structure/morphology of carbon deposits [42]. The amount of carbon deposition is insignificant for Ni crystallites sizes less than 10 nm and more than 100 nm and is greatest for Ni of about 20–30 nm in size [36]. On Ni particles of medium size (20–45 nm), the formation of carbon in the form of nanotubes prevails, and on small particles (<10 nm), amorphous carbon is typically found [36,42]. Carbon species (C_s) formed during DRM can be removed through reaction with labile lattice oxygen (O_L) of support and creating oxygen vacancies (V_o) that are replenished by the dissociative adsorption of CO₂ on the support (10) and (11) [42]:





The rate of this carbon removal route is influenced by redox properties of the support and the dimension of the metal–support interface through which the migration of oxygen species from the support to the surface of Ni particles occurs [36]. Co-interaction of Ni⁰ and Ce³⁺(OH) through MSI facilitates oxygen transfer in Ni/CeO₂ [43]. Note that the metal–support interface contains specific highly reactive species [44–48]. In particular, in SRM over low-loaded Ni/CeO₂ catalysts, it has been shown that the activation of water at interfacial Ni sites facilitates the generation of OH species and opens additional OH-assisted CO-formation pathways via the COH intermediate formed from chemisorbed C atoms and OH groups, hindering carbon accumulation and catalyst deactivation [44]. The clusters of Ni at the ceria step edge with highly cationic characters of interfacial Ni atoms were found to have an outstanding activity in dissociating all the reactant molecules (CH₄, H₂O, and CO₂) [45]. Therefore, for high activity and superior decoking catalyst capability, it is advantageous to stabilize the strongly anchored small nickel nanoparticles on a support with appropriate oxygen storage/transport characteristics [36,44].

Among reforming catalyst carriers (Al₂O₃, MgO, ZrO₂, La₂O₃, SiO₂, CeO₂, and their mixtures), CeO₂ has great advantages due to its unique structural characteristics, the redox property of the Ce⁴⁺/Ce³⁺ pair, and the accompanying dynamic and total oxygen storage capacity (OSC) [25,49]. To tailor support crystal structure and morphology, thermal stability, surface basicity, oxygen defects, and lability, ceria is modified by aliovalent (Mg²⁺, Gd³⁺, La³⁺, and Al³⁺), isovalent (Zr⁴⁺, Si⁴⁺, and Ti⁴⁺) or aliovalent/isovalent (Pr^{3+/4+}, Tb^{3+/4+}, and Mn^{2+/3+/4+}) dopants [42,50–55]. The oxygen vacancies in CeO₂ arising during doping can serve as sites to anchor the active component as well as to activate the oxygen-containing bond in the reaction reagents [56]. A doping additive can also affect the form of the stabilization of the active component by controlling the strength of the MSI as well as create new ways of reactant transformation. Compared to undoped CeO₂, Ce_{1-x}M_xO_y (M = Gd, La, Mg, x = 0–0.5; 1.5 ≤ y ≤ 2.0) materials have a larger surface area, smaller crystallite size, and improved thermal stability, which contributes to Ni's resistance to sintering and coking when used as support [53]. When the Ce/La ratio reached the optimum value (0.15), the Ce–La binary oxide had the highest CO₂ adsorption energy and demonstrated the best coke-removal performance [57]. By introducing in-ceria Zr as the dopant, the performance of Ni catalyst in DRM was enhanced due to a higher reducibility of the mixed-oxide support and hindering the particle sintering process of both Ni and ceria [58]. Thus, careful selection of the type and content of the dopant is necessary in order to achieve suitable physicochemical and functional properties of materials.

Ceria-based solid solutions not only act as carriers, but are increasingly used as Ni catalyst precursors [59–63]. In this case, the cations of the active component initially dissolve in the oxide lattice of the CeO₂-based support. When the solid solution is exposed to a reducing medium, the metal cations of the active component are reduced; the lattice oxygen is removed, and positively charged oxygen vacancies are formed in the lattice. Such an “exsolution” process is an effective approach to the formation of metal nanoparticles deposited on oxide surfaces [64–66]. In catalytic systems thus obtained, as a rule, a strong MSI is realized, which leads to high activity and stability of the catalyst [62,67,68]. Binary Ce–Ni–O systems are widely studied and applied for CO oxidation [69], water–gas-shift reaction [70], DRM [12], and autothermal reforming of ethanol (ATR of C₂H₅OH) [30]. It is known that the inclusion of Ni into the CeO₂ lattice introduces more defect sites and better OSC, ensuring the resistance of the catalyst to coking [31]. Ternary compounds Ce–M–Ni–O have been studied to a lesser extent. At the same time, the introduction of M strongly modifies the structure of nickel–cerium-based mixed oxides, changes the environment of active sites, and creates new Ni surface species [63]. Namely, results obtained on CeNi_xO_y (x = Ni/Ce, 0 < x ≤ 1) prepared by co-precipitation show coexisting nickel oxide and ceria modified by the insertion of Ni cations in its lattice, while on CeAl_zNi_xO_y they show a delay in the formation of NiO crystallites due to strong interaction between Al³⁺ and Ni²⁺ [63]. It

was established [59] that La- or Mg-containing samples, compared to $\text{Ce}_{0.8}\text{Ni}_{0.2}\text{O}_y$, have a strongly defective structure and smaller crystallite sizes.

The method of preparation for mixed oxides is also an important point, since it can affect the material genesis and the mechanism of catalyst deactivation under the reaction conditions. It was shown that, resulting from the combustion synthesis (CS) in comparison to the co-precipitation, a greater fraction of Ni cations was incorporated into the $\text{Ce}_x\text{Zr}_{1-x}\text{O}_2$ lattice-forming mixed metal oxides [31], and a smaller Ni particle size and stronger Ni-support interaction were realized [61]. At the same time, CS samples were more resistant to both Ni particle growth and coke formation, but suffered from Ni encapsulation by the support [31]. Great opportunities in the preparation of solid solutions are opened up by the polymerizable complex (PC) method [30,71,72]. Compared to samples obtained by impregnation, the Ni/CeO₂ catalysts obtained by the PC method were characterized by a smaller average CeO₂ crystallite size (5.5 vs. 11 nm), higher specific surface area (105 vs. 75 m²/g), defective structure, and reduced reducibility, and they were more resistant to the formation of carbonaceous deposits during the ATR of C₂H₅OH [30].

In this work, hydrogen production through the bi-reforming of methane was comprehensively studied over Ni catalysts derived from $(\text{CeM})_{1-x}\text{Ni}_x\text{O}_y$ solid solutions of different compositions (M = Al, La, Mg; M/Ce = 0–4; x = 0.2–0.8; y = 1.0–2.0). The choice of doping cations was based on the ability of these elements to provide different characteristics to the oxide matrix and strength of MSI, which is expected to affect the physicochemical and functional properties of catalysts. The role of dopant type (M = Al, La, Mg) in the catalyst genesis and properties were elucidated using X-ray fluorescence analysis, thermal analysis, N₂ adsorption, ex situ and in situ X-ray diffraction, Raman spectroscopy, high-resolution transmission electron microscopy, scanning electron microscopy, EDX analysis, and temperature-programmed hydrogen reduction and this provided novel insights about developing better catalysts. Careful control of the composition and activation conditions of Ni-Ce-containing solid solutions made it possible to create highly active and stable catalysts for hydrogen production through the bi-reforming of methane.

2. Results and Discussion

2.1. Characterization of Fresh Samples

The chemical composition and textural properties of fresh $(\text{CeM})_{1-x}\text{Ni}_x\text{O}_y$ samples are given in Table 1. The chemical composition of the samples is in good agreement with the theoretically defined values.

Three series of $(\text{CeM})_{1-x}\text{Ni}_x\text{O}_y$ samples were obtained using the polymerizable complex method, differing in the type (M = Al, La, Mg) and content (M/Ce = 0–4; x = 0.2; y = 1.0–2.0) of the dopant cation M, and one series based on an unmodified ceria, where the Ni/Ce molar ratio was varied over a wide range (0.01–4) and x was changed from 0.01 to 0.8.

When obtaining multicomponent solid solutions through the PC method (Figure 1), all metal cations are mixed at the molecular level in the water solution and then CA-complexes are homogeneously distributed in the gel and polymer resin. This preserves the initial stoichiometry of the molar ratio of cations in the final material, but does not exclude the coexistence of several amorphous or crystalline phases after the procedure of its thermal treatment [72].

Table 1. Chemical composition and textural properties of $(\text{CeM})_{1-x}\text{Ni}_x\text{O}_y$ samples.

Sample	Chemical Composition, wt.%			Textural Characteristics		
	Ce	M	Ni	$S_{\text{BET}}, \text{m}^2/\text{g}$	$V_p, \text{cm}^3/\text{g}$	D_p, nm
Unmodified CeO₂ CeO ₂	82.6	–	–	83	0.20	9.6
Without M						
Ce _{0.99} Ni _{0.01} O _{1.99} *	81.0	–	0.3	79	0.19	9.6
Ce _{0.95} Ni _{0.05} O _{1.95}	80.1	–	2.2	107	0.20	7.3
Ce _{0.9} Ni _{0.1} O _{1.9}	78.1	–	5.1	112	0.24	8.5
Ce _{0.8} Ni _{0.2} O _{1.8}	72.1	–	11.0	106	0.23	8.8
Ce _{0.7} Ni _{0.3} O _{1.7}	67.5	–	15.6	117	0.27	9.1
Ce _{0.3} Ni _{0.7} O _{1.3}	40.8	–	39.5	98	0.26	10.8
Ce _{0.2} Ni _{0.8} O _{1.2}	30.1	–	49.6	103	0.23	9.0
M = Al						
Ce _{0.6} Al _{0.2} Ni _{0.2} O _{1.7}	66.2	3.2	10.1	115	0.19	6.9
Ce _{0.4} Al _{0.4} Ni _{0.2} O _{1.6}	54.6	10.6	9.8	80	0.22	11.3
Ce _{0.2} Al _{0.7} Ni _{0.1} O _{1.5}	32.5	25.1	10.0	25	0.11	16.7
Al _{0.9} Ni _{0.1} O _{1.5}	–	46.3	9.9	20	0.11	22.0
M = La						
Ce _{0.6} La _{0.2} Ni _{0.2} O _{1.7}	57.4	14.2	9.8	100	0.31	12.3
Ce _{0.4} La _{0.4} Ni _{0.2} O _{1.6}	36.5	36.2	9.4	48	0.18	15.6
Ce _{0.2} La _{0.6} Ni _{0.2} O _{1.5}	14.8	58.6	9.2	34	0.15	18.1
La _{0.8} Ni _{0.2} O _{1.4}	–	74.2	10.0	24	0.10	17.1
M = Mg						
Ce _{0.6} Mg _{0.2} Ni _{0.2} O _{1.6}	67.0	2.9	9.9	93	0.25	10.8
Ce _{0.4} Mg _{0.4} Ni _{0.2} O _{1.4}	57.0	9.9	9.2	36	0.15	17.0
Ce _{0.2} Mg _{0.7} Ni _{0.1} O _{1.2}	37.7	25.4	9.7	23	0.10	17.7
Mg _{0.9} Ni _{0.1} O	–	54.1	10.2	43	0.22	20.4

*—A formula used to designate the samples, where the coefficients indicate the mole fraction (usually rounded to tenths) of each element in the composition of the material.

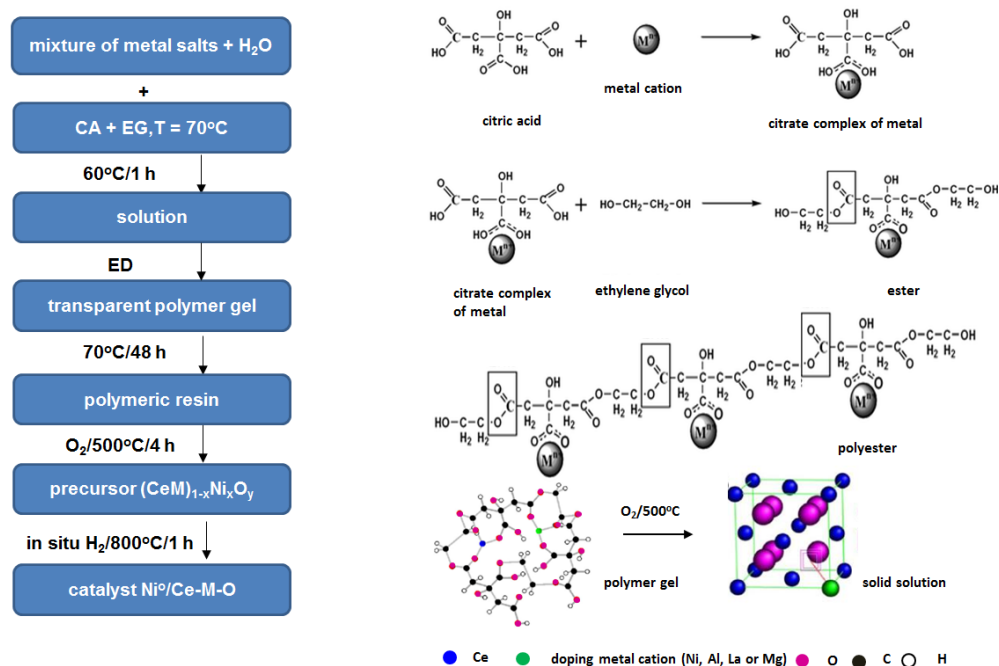


Figure 1. Scheme for the synthesis of $(\text{CeM})_{1-x}\text{Ni}_x\text{O}_y$ ($\text{M} = \text{Al}, \text{La}, \text{Mg}$) solid solutions used as catalyst precursors in the polymerizable complex method.

The TA method was used to study the genesis of materials from a gel into a solid phase during thermal treatment. As typical example, Figure 2a illustrates the TG, DTG, and DTA curves for a $\text{Ce}_{0.8}\text{Ni}_{0.2}\text{O}_{1.8}$ sample. There are three main peaks on the DTG curve. The first peak at $T < 200\text{ }^\circ\text{C}$ is accompanied by an endothermic effect and can be associated with the desorption of water and volatile organic compounds. The second peak at $T \approx 300\text{ }^\circ\text{C}$ and the third peak at $400\text{ }^\circ\text{C} < T < 600\text{ }^\circ\text{C}$ match well with the exothermic events observed in the DTA curve and can be assigned to multistage oxidation of the polymer matrix.

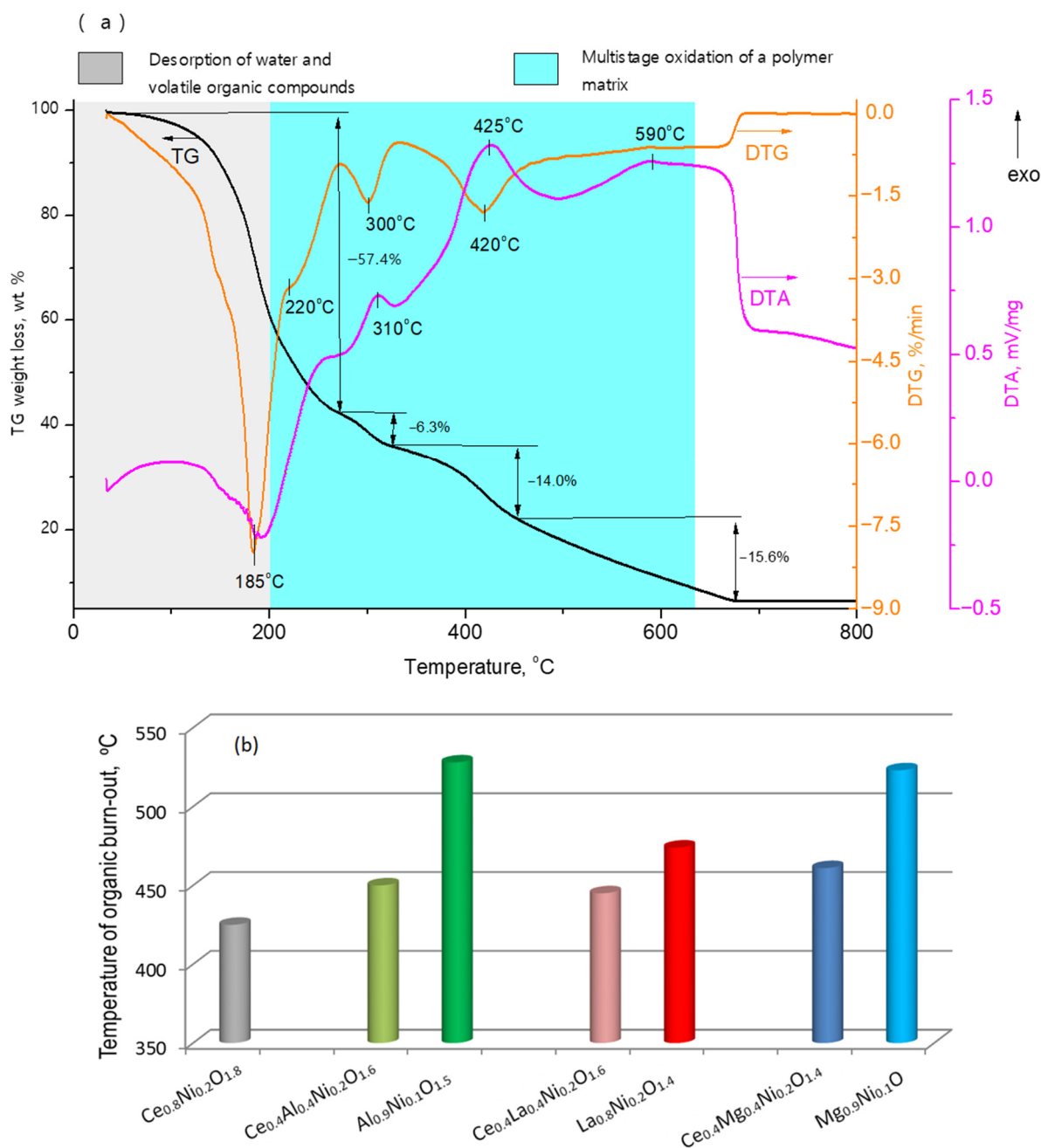


Figure 2. Thermal analysis of the gel-precursor for $\text{Ce}_{0.8}\text{Ni}_{0.2}\text{O}_{1.8}$ sample (a) and effect of oxide matrix composition on the temperature of organics burn-out during TA of gel-precursors (b).

For $(\text{CeM})_{1-x}\text{Ni}_x\text{O}_y$ samples, compared to $\text{Ce}_{1-x}\text{Ni}_x\text{O}_y$, the profiles of the TG, DTG, and DTA curves have the similar behavior, but the temperature of organics burn-out shifts to the high-temperature region (Figure 2b). Thus, the introduction of M does not lead to a change in the sequence of decomposition of the organic matrix but rather slows it down.

This effect increases in the series $\text{La} < \text{Al} \approx \text{Mg}$ and can be explained by differences in (i) the resistance of citrate–metal complexes to degradation and (ii) the catalytic activity of metals in the oxidation of organic compounds. The stability of citrate metal complexes increases in the series Mg ($\lg k_1 = 4.0$) $<$ Ni ($\lg k_1 = 5.4$) $<$ Ce ($\lg k_1 = 7.4$) $<$ Al ($\lg k_1 = 8.0$) $<$ La ($\lg k_1 = 8.4$) [73], which has no correlation with the temperature of organic matrix degradation (Figure 2b). Apparently, the presence of a redox $\text{Ce}^{4+}/\text{Ce}^{3+}$ pair accelerates the oxidation reactions of organic residues, which reduces their burnout temperature with increasing content of Ce in the gel. Indeed, cerium-free samples have the highest organic matrix burnout temperature (Figure 2b). Note that, according to [74], hindered organic decomposition has a positive effect on the dispersion of the crystalline phase due to the capping around the particles and their protection from sintering. Accordingly, it can be expected that differences in the parameters of the thermal genesis of materials will affect their textural and/or structural properties.

The porous structure of the catalysts is formed under the condition of burnout of the organic matrix, accompanied by the release of gaseous combustion products. Data on low-temperature nitrogen adsorption indicate that $(\text{CeM})_{1-x}\text{Ni}_x\text{O}_y$ are mesoporous materials. As evidenced by the type IV adsorption isotherm with an H3 hysteresis loop at $P/P_0 > 0.6$ (Figure 3), the samples have predominantly textural mesoporosity (pores between primary particles) [75,76]. The specific surface area of the $\text{Ce}_{1-x}\text{Ni}_x\text{O}_y$ samples practically does not change when the mole fraction of Ni varies within 0.05–0.8 and amounts to $110 \pm 10 \text{ m}^2/\text{g}$ (Table 1), which represents a typical value for the Ce–Ni–O system [12,77]. It is noteworthy that, unlike samples obtained by impregnation, even at a high nickel content, the S_{BET} and V_p of the samples are higher than for unmodified ceria with $S_{\text{BET}} = 83 \text{ m}^2/\text{g}$ (Figure 4a). In particular, at $x = 0.3$ (15 wt.% Ni) S_{BET} is equal to 117 and 65 for samples obtained by the polymerizable complex method and impregnation, respectively. The specific surface area and total pore volume of $(\text{CeM})_{1-x}\text{Ni}_x\text{O}_y$ samples increased with decreasing M/Ce molar ratio (Table 1, Figure 4b). This trend intensifies in the series of M: $\text{Mg} < \text{La} < \text{Al}$. The average pore diameter depends on the composition of the material and varies from 7.3 to 22 nm. It increases with an increase in the M/Ce molar ratio. There are inhibition as well as promotion effects from dopants on the textural characteristics. In our case, the incorporation of Ni cations improves the textural properties of CeO_2 , while for $(\text{CeM})_{1-x}\text{Ni}_x\text{O}_y$ samples only for samples with M/Ce equal to 0.3, the textural characteristics are higher than for unmodified ceria. The resultant dependence of the textural properties of the samples upon their chemical composition may reflect the effects of dopant cations (Ni, Al, La, and Mg) of ceria on the sintering mode of the material and, consequently, phase dispersion and material porosity [77–79].

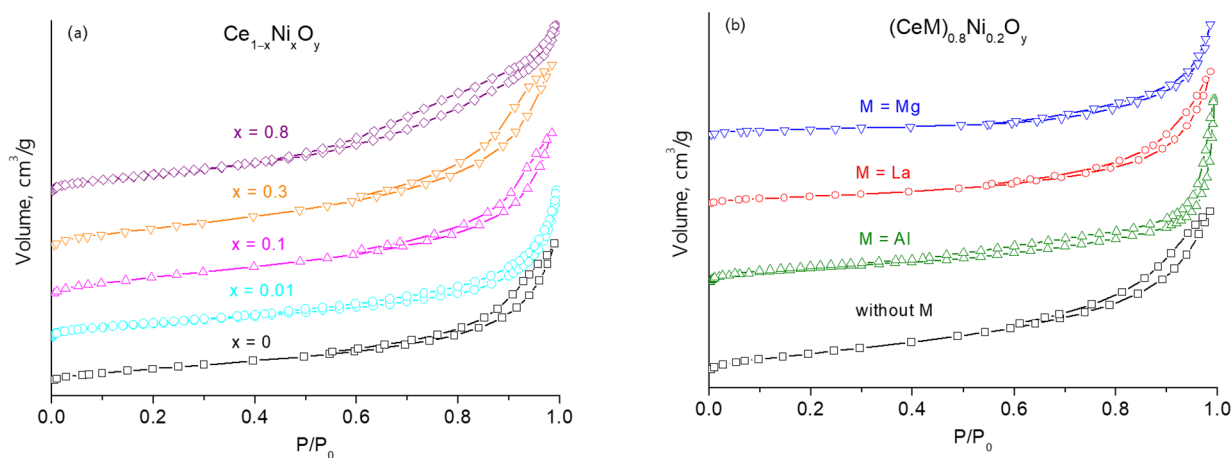


Figure 3. N_2 adsorption–desorption isotherms for $(\text{CeM})_{1-x}\text{Ni}_x\text{O}_y$ ($\text{M} = \text{Al}, \text{La}, \text{Mg}$) samples: effect of Ni molar fraction (a) and M type (b). (b)—M/Ce molar ratio is equal to 1. Isotherms are shifted relative to each other along the y-axis.

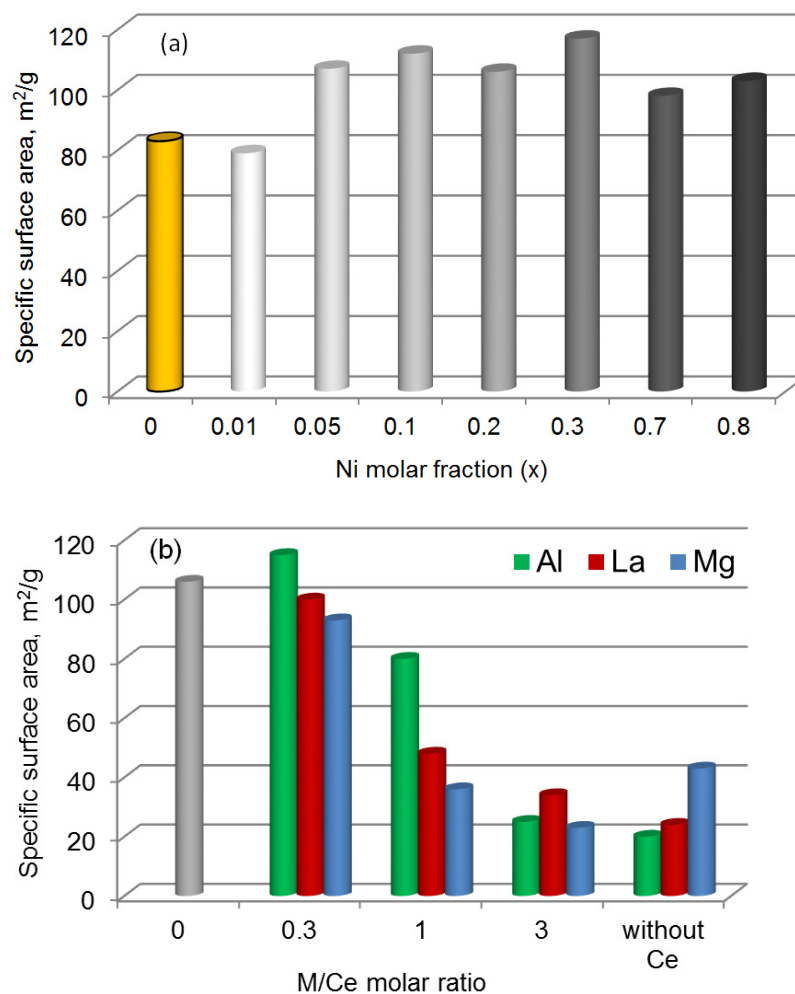


Figure 4. Effect of Ni molar fraction (a) and M/Ce molar ratio (b) on the specific surface area of (CeM)_{1-x}Ni_xO_y (M = Al, La, Mg) samples: (a) M/Ce molar ratio is equal to 0; (b) Ni molar fraction is equal to 0.2.

The morphological properties of the samples are close. They are aggregates of spongy particles (Figure 5). The formation of their porous macrostructure occurs under conditions of intense gas evolution due to the spontaneous burnout of the organic matrix.

Table 2 demonstrates the phase and structure data for (CeM)_{1-x}Ni_xO_y samples. X-ray diffraction analysis indicates the presence of a CeO₂-based cubic phase in all Ce-containing samples (Figure 6). The only exception is the Ce_{0.2}Al_{0.7}Ni_{0.1}O_{1.5} sample, for which the XRD pattern of an amorphous phase is observed. The Ni-containing phase is observed at a high nickel content (x = 0.7, 0.8) and also at M = Mg. In the first case, highly dispersed particles of NiO with an average size of ~5 nm are formed, and in the second case, a solid solution of NiO-MgO with a particle size of 4–8 nm is observed (Table 2, Figure 6). In the cerium-free samples—La_{0.8}Ni_{0.2}O_{1.4} and Mg_{0.9}Ni_{0.1}O—the La₂O₂CO₃ and NiO-MgO solid solution phases are observed, respectively, while the Al_{0.9}Ni_{0.1}O_{1.5} sample is X-ray amorphous.

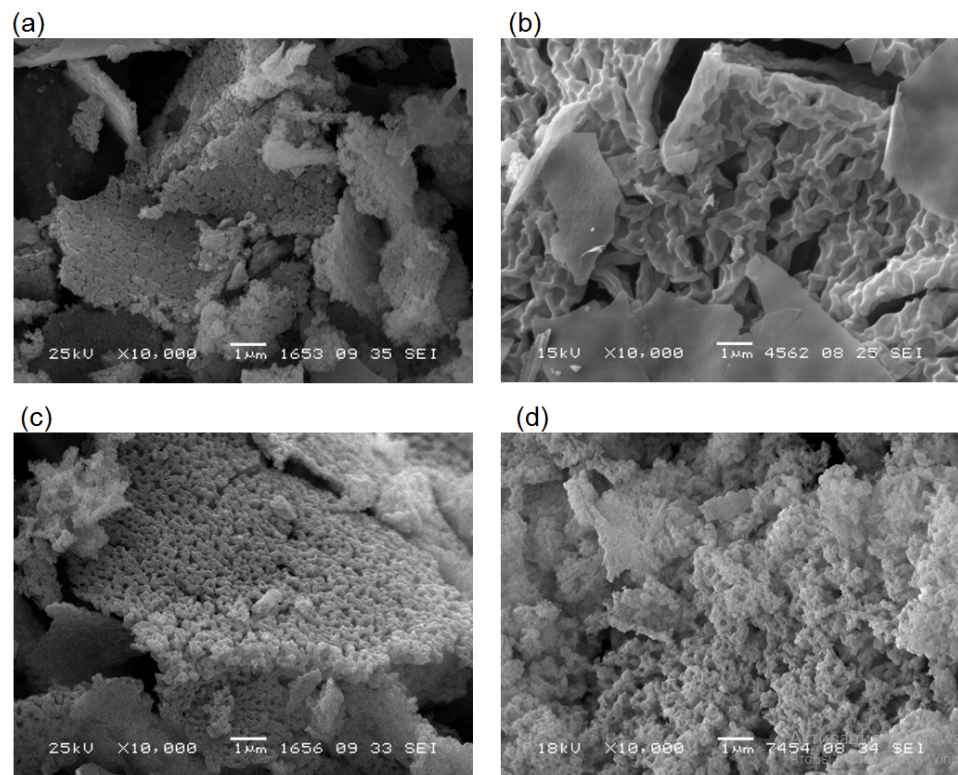


Figure 5. SEM images of $(\text{CeM})_{0.8}\text{Ni}_{0.2}\text{O}_y$ samples without M (a), M = Al (b), La (c), and Mg (d). (b–d) M/Ce molar ratio is equal to 1.

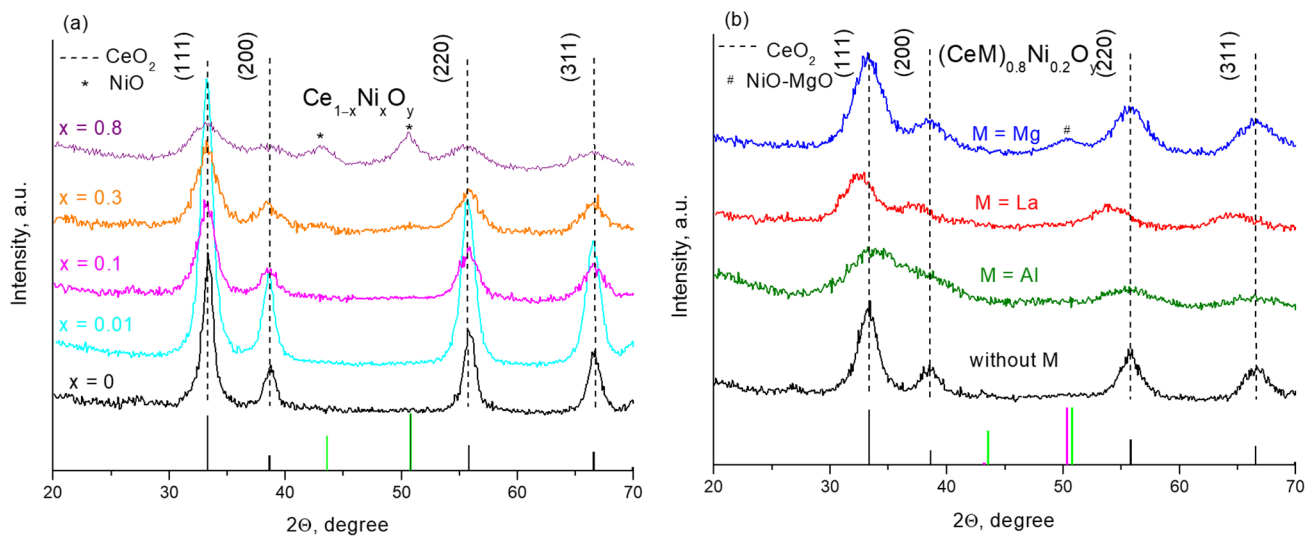


Figure 6. XRD patterns for $(\text{CeM})_{1-x}\text{Ni}_x\text{O}_y$ (M = Al, La, Mg) samples: effect of Ni molar fraction (a) and M type (b). (b) M/Ce molar ratio is equal to 1. The standard patterns of CeO_2 (ICDD 43–1002, black bars), NiO (ICDD 44–1159, green bars), and MgO (ICDD 45–0946, magenta bars) are shown.

Table 2. Phase composition and structural properties of $(\text{CeM})_{1-x}\text{Ni}_x\text{O}_y$ samples.

Sample	XRD Data		Raman Spectroscopy Data	
	Phase Composition	a , nm	CSR, nm	I_{570}/I_{465}
Unmodified CeO₂ CeO ₂	CeO ₂	0.5412	11.0	0
Without M				
Ce _{0.99} Ni _{0.01} O _{1.99}	CeO ₂	0.5414	9.5	0
Ce _{0.95} Ni _{0.05} O _{1.95}	CeO ₂	0.5416	8.5	0.4
Ce _{0.9} Ni _{0.1} O _{1.9}	CeO ₂	0.5413	6.5	0.6
Ce _{0.8} Ni _{0.2} O _{1.8}	CeO ₂	0.5412	5.5	1.0
Ce _{0.7} Ni _{0.3} O _{1.7}	CeO ₂	0.5414	5.5	1.4
Ce _{0.3} Ni _{0.7} O _{1.3}	CeO ₂	0.5412	3.2	7.4
	NiO		5.0	
Ce _{0.2} Ni _{0.8} O _{1.2}	CeO ₂	0.5405	2.6	10.8
	NiO		5.5	
M = Al				
Ce _{0.6} Al _{0.2} Ni _{0.2} O _{1.7}	CeO ₂	0.5409	4.5	1.1
Ce _{0.4} Al _{0.4} Ni _{0.2} O _{1.6}	CeO ₂	0.5412	2.8	4.0
Ce _{0.2} Al _{0.7} Ni _{0.1} O _{1.5}	X-ray amorphous phase	–	–	–
Al _{0.9} Ni _{0.1} O _{1.5}	X-ray amorphous phase	–	–	–
M = La				
Ce _{0.6} La _{0.2} Ni _{0.2} O _{1.7}	CeO ₂	0.5468	6.0	1.4
Ce _{0.4} La _{0.4} Ni _{0.2} O _{1.6}	CeO ₂	0.5553	4.0	–
Ce _{0.2} La _{0.6} Ni _{0.2} O _{1.5}	CeO ₂	0.5661	4.0	–
La _{0.8} Ni _{0.2} O _{1.4}	La ₂ O ₂ CO ₃	–	–	–
M = Mg				
Ce _{0.6} Mg _{0.2} Ni _{0.2} O _{1.6}	CeO ₂	0.5408	5.5	1.1
	MgO-NiO	0.4182	4.0	
Ce _{0.4} Mg _{0.4} Ni _{0.2} O _{1.4}	CeO ₂	0.5410	3.5	0.8
	MgO-NiO	0.4204	3.6	
Ce _{0.2} Mg _{0.7} Ni _{0.1} O _{1.2}	CeO ₂	0.5414	5.5	1.4
	MgO-NiO	0.4212	8.5	
Mg _{0.9} Ni _{0.1} O	MgO	0.4222	18.0	–

The structural characteristics of a CeO₂-based phase depend on the content ($x = 0.001\text{--}0.8$, $M/\text{Ce} = 0\text{--}4$), ionic radius ($r_{\text{Ni}^{2+}} = 0.69 \text{ \AA}$, $r_{\text{Al}^{3+}} = 0.68 \text{ \AA}$, $r_{\text{La}^{2+}} = 1.16 \text{ \AA}$, $r_{\text{Mg}^{2+}} = 0.72 \text{ \AA}$), and degree of oxidation (2+ for Ni and Mg cations, 3+ for Al and La cations) of the dopant. It can be seen that in case of doping cations (Ni, Al, Mg) with a radius smaller than that of Ce⁴⁺ ($r_{\text{Ce}^{4+}} = 0.97 \text{ \AA}$), the unit cell parameter a of cubic CeO₂-based phase is 0.5412 ± 0.0004 nm and differs little from that for unmodified CeO₂. On the contrary, in the case of La, which has a larger radius, a noticeable increase in the unit cell parameter is observed (Table 2), which can indicate the incorporation of La³⁺ cations into the ceria lattice. For all samples, a decrease in the size of crystallites is observed in comparison with unmodified ceria. This effect is enhanced with increasing x , increasing M/Ce ratio and in the series La→Mg→Al (Figure 7), which correlates with the difficulty of burnout of the organic matrix (Figure 2b) and indicates the inhibitory effect of the cations introduced into the ceria structure on the growth of crystallites and an increase in the thermal stability to sintering of $(\text{CeM})_{1-x}\text{Ni}_x\text{O}_y$ samples.

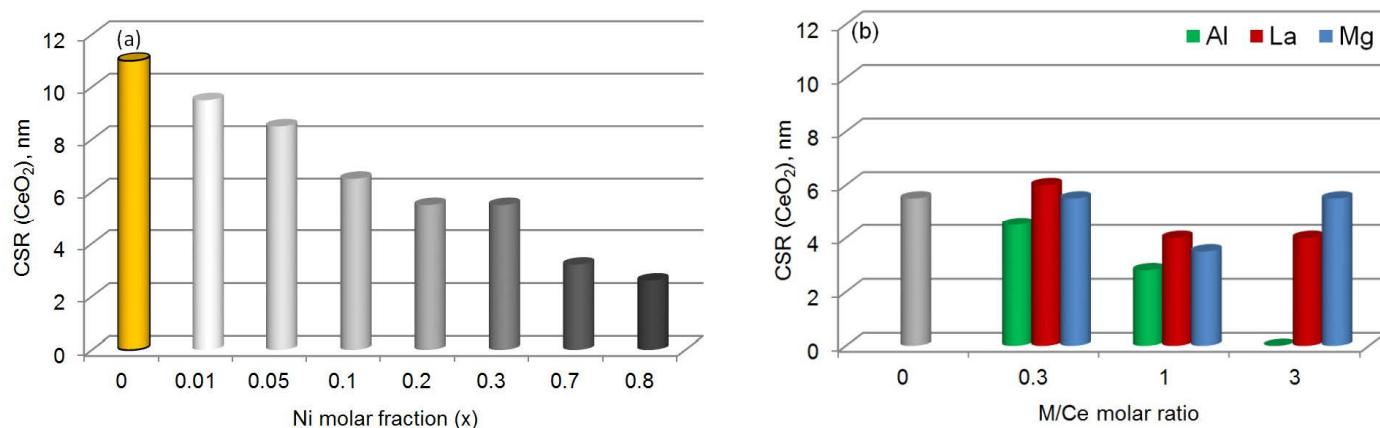


Figure 7. Effect of Ni molar fraction (a) and M/Ce molar ratio (b) on the CSR value of a CeO₂-based phase in (CeM)_{1-x}Ni_xO_y (M = Al, La, Mg) samples. (a) M/Ce molar ratio is equal to 0; (b) Ni molar fraction is equal to 0.2.

In the case of (CeLa)_{1-x}Ni_xO_y samples, the absence of a nickel-containing phase, a decrease in the particle size, and an increase in the lattice parameter of the CeO₂-based phase clearly points to the formation of a solid solution. For the Ce_{1-x}Ni_xO_y and (CeAl)_{1-x}Ni_xO_y-series, no Ni-containing phases were observed either, and the CSR size for CeO₂ decreases with increasing x or M/Ce ratio. However, for these samples, the cell parameters remain virtually unchanged (Table 2). Based on the XRD data, it can be assumed that a solid solution is also formed in this case. But since the Ce³⁺/Ce⁴⁺ ratio increases with decreasing particle size [80], an increase in the concentration of Ce³⁺ with bigger ionic radius ($r_{\text{Ce}^{3+}} = 1.14 \text{ \AA}$) compensates for the expected decrease in the cell parameter of a CeO₂-based solid solution. According to [80], the cell parameter *a* increases from 0.541 to 0.554 Å as the CeO₂ particle size decreases from 70 to 3 nm. It was also shown [70] that differences in the formal charge of Ni²⁺ and Ce⁴⁺ promote the formation of oxygen vacancies and, as a consequence, lattice expansion. Less obvious from the XRD data is the formation of a solid solution for the (CeMg)_{1-x}Ni_xO_y-series. In this case, although there is a decrease in the size of crystallites of the CeO₂-based phase, a NiO-MgO solid solution is present in the sample. Its unit cell parameter has values in the range of 0.4182–0.4212 nm, which lies between the values characteristic of individual oxides (0.4177 for NiO and 0.4213 for MgO) and increases with increasing Mg content in the sample (Table 2). This may indicate only a partial incorporation of Ni²⁺ and Mg²⁺ doping cations into the ceria lattice. The solubility limit of a dopant in the ceria lattice with the formation of a solid solution depends on the type of dopant and the method of its introduction. For Ce_{1-x}M_xO_y, a single-phase fluorite-like system is observed up to x = 0.1–0.5 for M = Ni [69,81,82], x = 0.6 for M = La [83–85] and x = 0.5–0.9 for M = Mg [86,87]. In addition, among the studied dopants (M = Al, La, and Mg), the Mg cations are characterized by the lowest stability of citrate complexes, which probably contributes to their less-successful entry into the ceria lattice.

Raman spectroscopy data provide additional information about the structural properties of the obtained samples (Table 2, Figure 8).

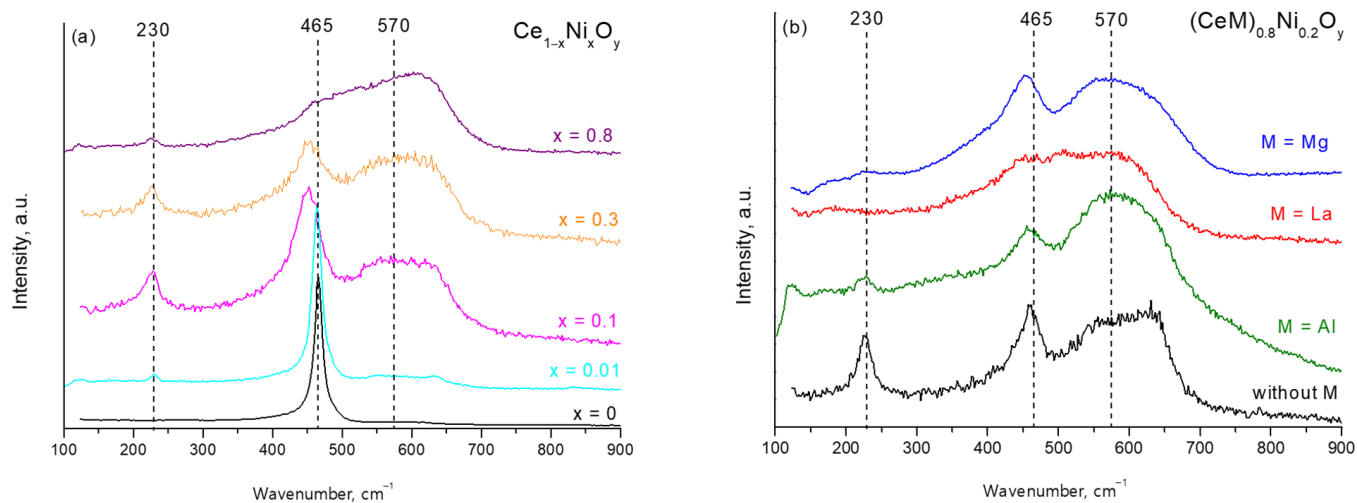


Figure 8. Raman spectra for $(\text{CeM})_{1-x}\text{Ni}_x\text{O}_y$ ($M = \text{Al}, \text{La}, \text{Mg}$) samples: effect of Ni molar fraction (a) and M type (b). (b) M/Ce molar ratio is equal to 1.

The spectrum of unmodified CeO_2 is characterized by one strong band at 465 cm^{-1} , which is due to the F2g vibration mode of the cubic fluorite structure [88,89]. In addition, it also exhibits two weak bands at about 250 and 600 cm^{-1} , which can be attributed to the non-degenerate transverse and longitudinal optical phonon modes of CeO_2 , respectively [90]. The Raman spectral features of the $(\text{CeM})_{1-x}\text{Ni}_x\text{O}_y$ samples were greatly affected by the content and type of dopant (Figure 8). For these samples, Raman spectra also include main bands at $452\text{--}464 \text{ cm}^{-1}$ and two weak bands at 230 cm^{-1} and $550\text{--}650 \text{ cm}^{-1}$, which can be attributed to the displacement of oxygen atoms from their ideal fluorite lattice positions [91] and the presence of defects such as oxygen vacancies [92]. This shows [93] that the emergence of the band at about 560 cm^{-1} (oxygen vacancies) results from the different oxidation state of the dopant compared to that of Ce^{4+} , while the band at about 600 cm^{-1} is caused by the different ionic radius of the dopant compared to that of Ce^{4+} . The I_{570}/I_{465} ratio, used to estimate the concentration of oxygen vacancies in a material [94], increases with increasing x , increasing M/Ce ratio, and in the series $\text{Mg} \rightarrow \text{Al} \rightarrow \text{La}$ (Table 2). The higher the I_{570}/I_{465} , the more oxygen vacancies in the material are formed. In addition, a shift ($465 \rightarrow 452 \text{ cm}^{-1}$) of the position of the main band in Raman spectra for $(\text{CeM})_{1-x}\text{Ni}_x\text{O}_y$ samples compared to the position of this band for pure CeO_2 was noted. This indicates a change in the binding energies due to the incorporation of Ni^{2+} and M^{n+} cations into the lattice of CeO_2 and confirms the formation of a solid solution. The considerable broadening of the bands observed for $(\text{CeM})_{1-x}\text{Ni}_x\text{O}_y$ (Figure 8) could be attributed to the reduction in phonon lifetime due to the decrease in grain size [88], which correlates well with XRD data (Figure 6). Significant deformation of the spectrum shape for La-containing samples at $\text{La}/\text{Ce} \geq 1$ points to a substantial rearrangement of the oxide structure compared to that of unmodified ceria. It was demonstrated [95] that with the increase of La concentration in $\text{Ce}_{1-x}\text{La}_x\text{O}_y$, the Raman spectra are progressively broadened and shifted to lower energy (from 464 cm^{-1} ($\text{La} = 0\%$) to 458 cm^{-1} ($\text{La} = 20\%$)). These effects agree with the formation of homogeneous La-doped CeO_2 solid solutions.

The study of the nanostructure of the $(\text{CeM})_{1-x}\text{Ni}_x\text{O}_y$ by TEM shows that the samples are represented by particles of two types: (1) thin polycrystalline plates, from 100 nm to several microns in length and $10\text{--}20 \text{ nm}$ in width; (2) small, irregularly shaped polycrystalline agglomerates up to 100 nm in size. According to the EDX data, the composition of all particles is close to the declared one. The size of primary crystallites is very small (Figure 9a–d). For example, at $x = 0.2$ and $\text{M}/\text{Ce} = 1$ it is equal $1.5\text{--}2.5 \text{ nm}$ for $M = \text{Al}$, $3\text{--}5 \text{ nm}$ for $M = \text{La}$ or Mg , and $5\text{--}8 \text{ nm}$ for the sample without M. Analysis of the interplanar distances measured from the high-resolution images and microdiffraction patterns reveal

the presence of a fluorite phase reflections corresponding to $d_{111}\text{CeO}_2$ (0.312 nm), $d_{200}\text{CeO}_2$ (0.271 nm) and $d_{220}\text{CeO}_2$ (1.913 nm). Also, in the case of the $(\text{CeMg})_{1-x}\text{Ni}_x\text{O}_y$ sample, the reflection at 0.211 nm corresponding to d_{200} of NiO-MgO particles is clearly visible in the electron diffraction pattern. In the $\text{Ce}_{1-x}\text{Ni}_x\text{O}_y$ and $(\text{CeLa})_{1-x}\text{Ni}_x\text{O}_y$ samples, only solitary highly dispersed NiO particles can be found on the surface of the samples with a typical interplanar distance of 0.209 nm corresponding to ($d_{200}\text{NiO}$). In the case of $M = \text{Al}$, no reflections that would correspond to Ni-containing phases are visible. EDX mapping shows a uniform distribution of elements in the studied samples (Figure 9, e–h) implying that even in the $(\text{CeMg})_{1-x}\text{Ni}_x\text{O}_y$ sample, there is a very intense mixing of crystallites of the Ce-containing phase and Ni(Mg)O nanocrystallites, which, under imaging conditions at selected magnification, does not allow one to distinguish inhomogeneities of the local composition.

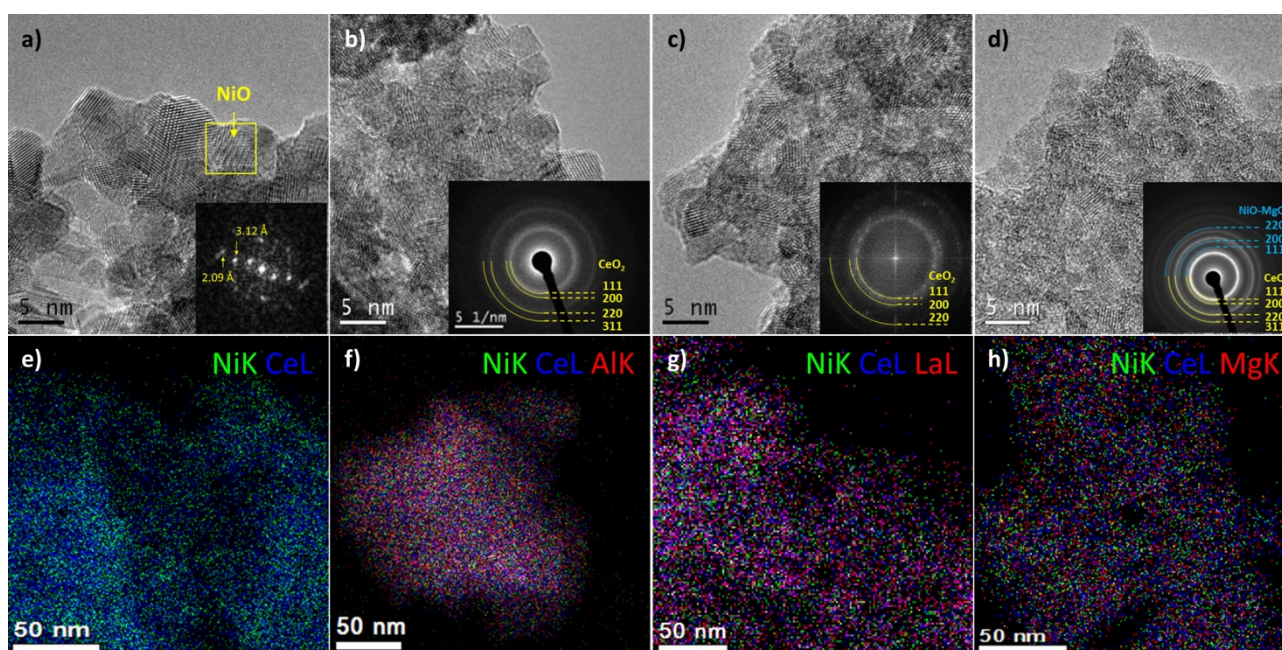


Figure 9. HRTEM pictures (a–d) and EDX mapping (f–h) of $\text{Ce}_{0.8}\text{Ni}_{0.2}\text{O}_y$ (a,e) and $(\text{CeM})_{0.8}\text{Ni}_{0.2}\text{O}_y$ ($M = \text{Al}$ (b,f)), La (c,g), Mg (d,h) samples. $M/\text{Ce} = 1$.

Thus, solid solutions of various chemical compositions based on the cubic structure of ceria with a very-fine crystallite size were actually obtained. Both nickel and M cations were inserted into the structure of ceria through the synthesis of $(\text{CeM})_{1-x}\text{Ni}_x\text{O}_y$ materials using the polymerizable complex method. This led to a significant decrease in the size of crystallites, an increase in the defectiveness of the material, and the formation of oxygen vacancies. Traces of highly dispersed Ni-containing species were also formed. This trend is intensified with an increase in the Ni content and with the use of Mg as a dopant. In the latter case, a MgO-NiO solid solution is formed. For the formation of catalytically active Ni^0 nanoparticles, the appropriate activation of $(\text{CeM})_{1-x}\text{Ni}_x\text{O}_y$ materials is needed.

2.2. Activation of Samples

As a rule, to activate nickel reforming catalysts, samples were reduced at a temperature of 600–800 °C for 1–3 h [37,96,97]. In order to study the features of the reduction of $(\text{CeM})_{1-x}\text{Ni}_x\text{O}_y$ samples, methods of temperature-programmed hydrogen reduction (Figures 10 and 11) and in situ XRD (Figures 12 and 13) were applied. On the TPR-H₂ curves of unmodified ceria, two regions of hydrogen consumption can be distinguished: in the temperature ranges of 100–600 °C (a peak maximum at $T = 500$ °C) and 600–1000 °C (a peak maximum at $T = 880$ °C), which are due to the reduction of cations Ce^{4+} localized on the surface and in the volume of particles, respectively [52,98]. The reduction profile of $(\text{CeM})_{1-x}\text{Ni}_x\text{O}_y$ samples depends upon the amount of introduced nickel (Figure 10a) as well as the type and content of M (Figure 10b).

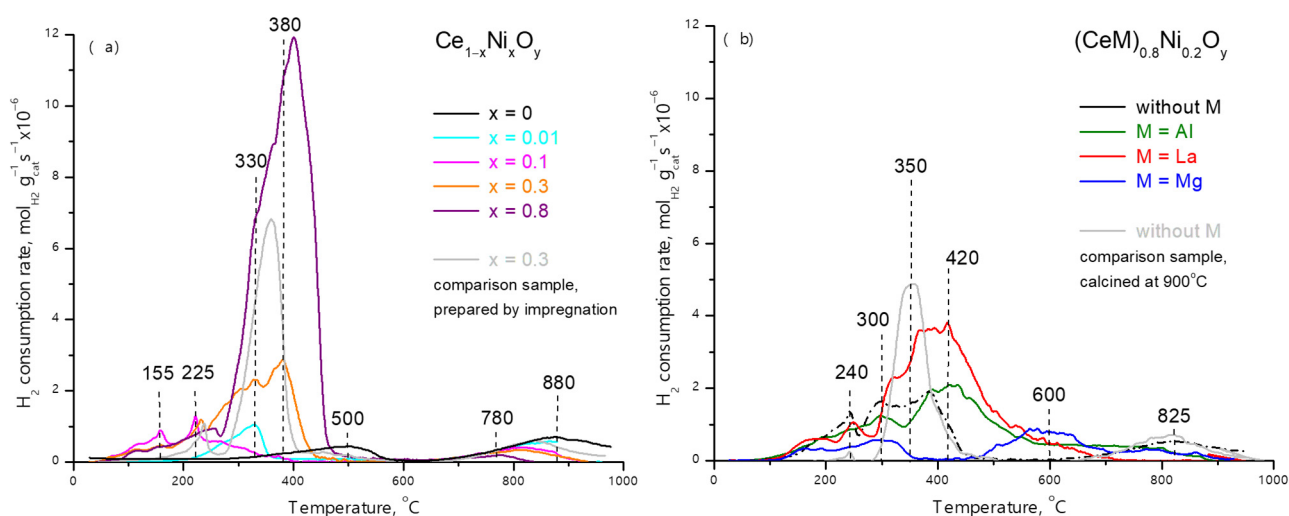


Figure 10. H₂-TPR profiles of $(\text{CeM})_{1-x}\text{Ni}_x\text{O}_y$ (M = Al, La, Mg) samples: effect of Ni molar fraction (a) and M type (b). (b) M/Ce molar ratio is equal to 1.

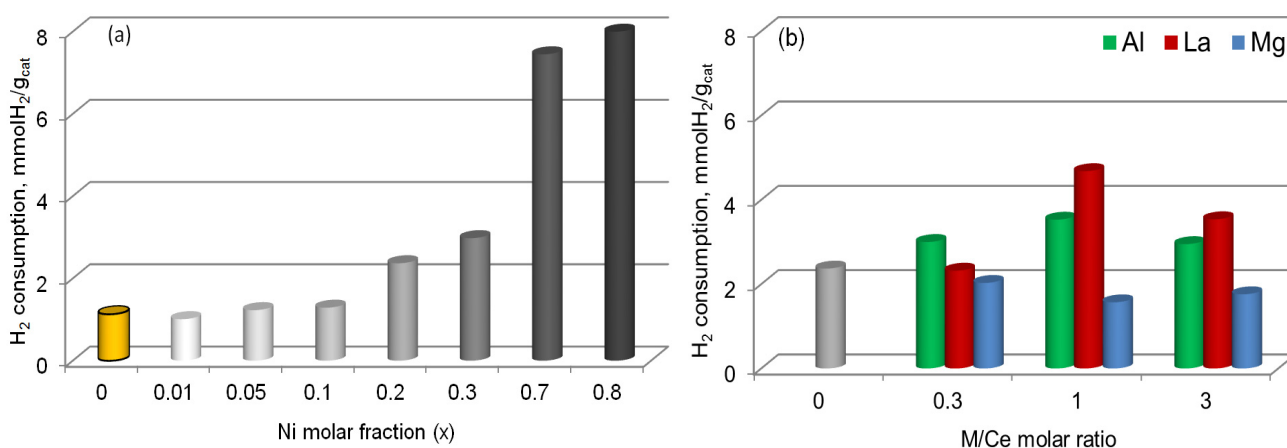


Figure 11. The effect of Ni molar fraction (a) and M/Ce molar ratio (b) on the total H₂ consumption rate. (a) M/Ce molar ratio is equal to 0; (b) Ni molar fraction is equal to 0.2.

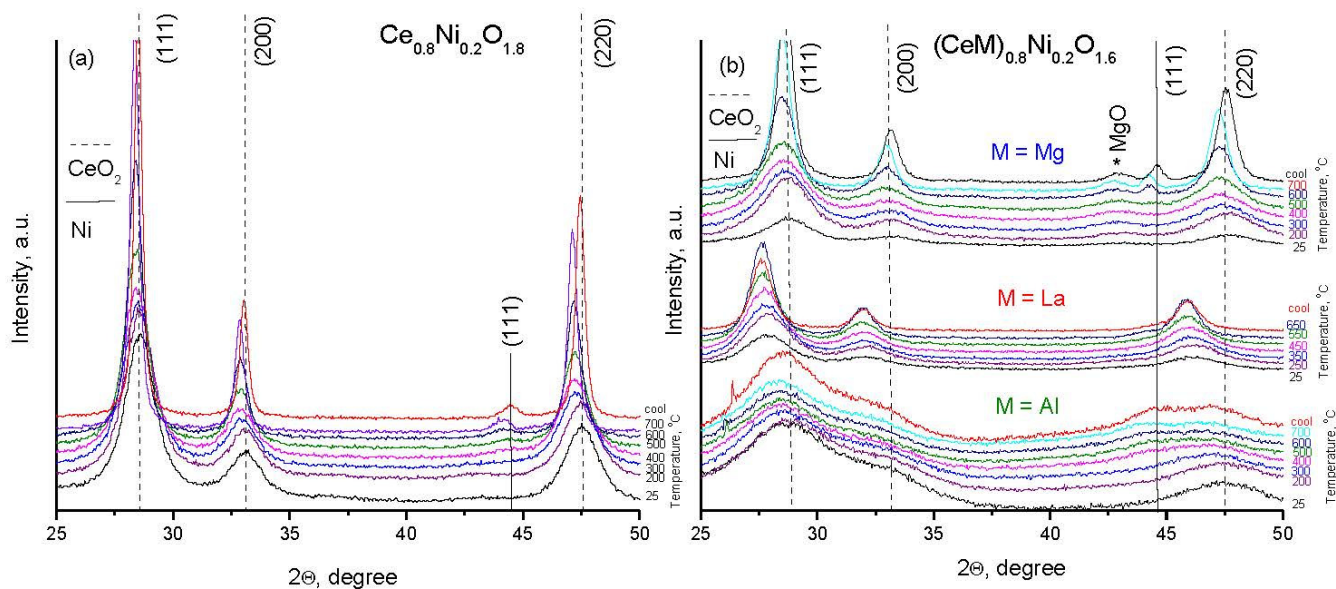


Figure 12. In situ XRD patterns for $(\text{CeM})_{1-x}\text{Ni}_x\text{O}_y$ samples under reduction in a 30% H_2 /70% He mixture as a function of temperature: (a) $\text{Ce}_{0.8}\text{Ni}_{0.2}\text{O}_{1.8}$, (b) $\text{Ce}_{0.4}\text{M}_{0.4}\text{Ni}_{0.2}\text{O}_y$. Arrows indicate the shift in the reflection (220) of the CeO_2 phase due to doping with lanthanum cations.

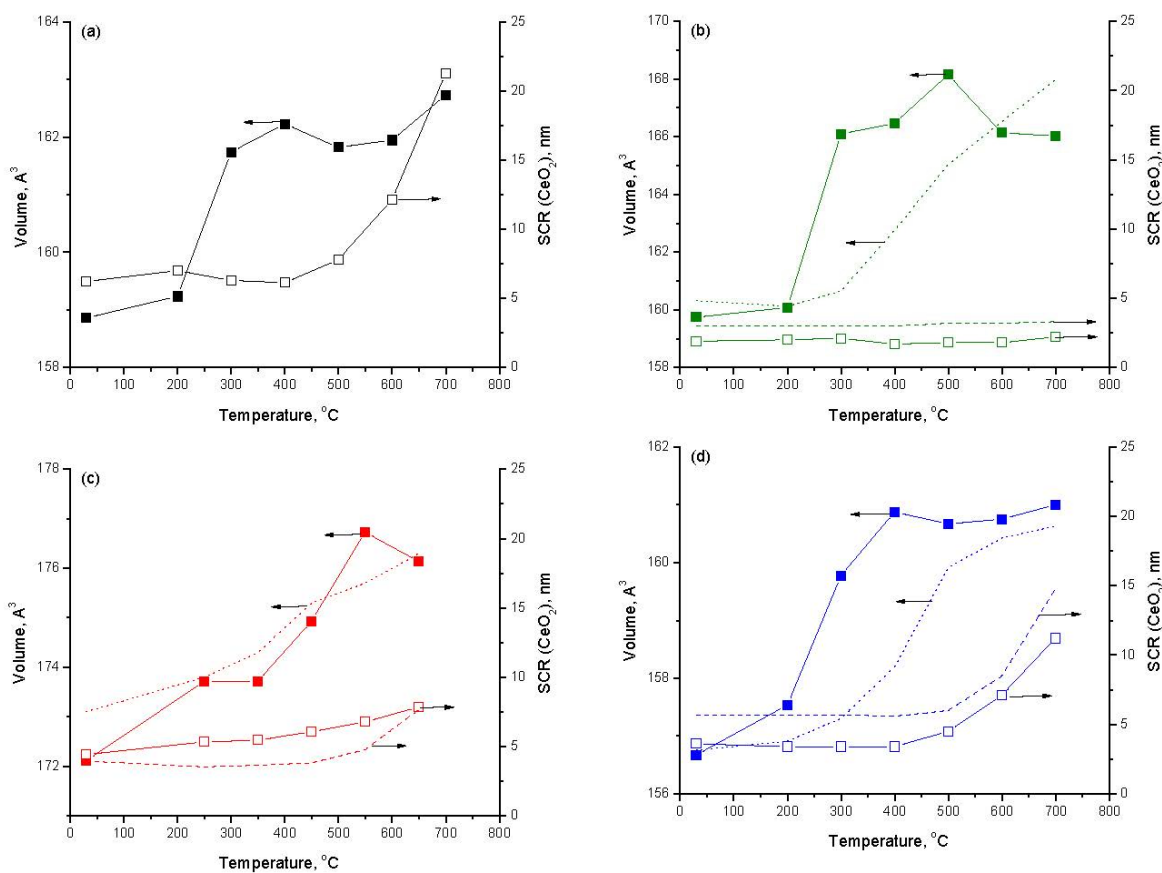
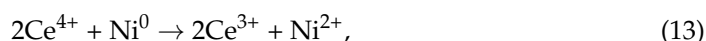
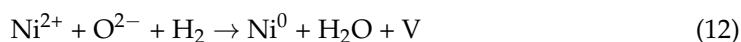


Figure 13. Evolution of the unit cell volume and CSR of CeO_2 -based solid solution during the reduction of $(\text{CeM})_{1-x}\text{Ni}_x\text{O}_y$ samples. (a) $\text{Ce}_{0.8}\text{Ni}_{0.2}\text{O}_{1.8}$; (b) $\text{Ce}_{0.4}\text{Al}_{0.4}\text{Ni}_{0.2}\text{O}_{1.6}$, $\text{Ce}_{0.5}\text{Al}_{0.5}\text{O}_{1.75}$; (c) $\text{Ce}_{0.4}\text{La}_{0.4}\text{Ni}_{0.2}\text{O}_{1.6}$, $\text{Ce}_{0.5}\text{La}_{0.5}\text{O}_{1.75}$; (d) $\text{Ce}_{0.4}\text{Mg}_{0.4}\text{Ni}_{0.2}\text{O}_{1.4}$, $\text{Ce}_{0.5}\text{Mg}_{0.5}\text{O}_{1.5}$. Dash and dot lines refer to nickel-free samples.

For $Ce_{1-x}Ni_xO_y$ -series, three regions of hydrogen consumption can be observed: low-temperature ($T < 250\text{ }^\circ\text{C}$), medium ($250 < T < 500\text{ }^\circ\text{C}$), and high-temperature ($T > 550\text{ }^\circ\text{C}$). In the low-temperature region, weak consumption of H_2 is observed, the intensity and position of which is practically independent on the Ni content. The two peaks with maxima at $\sim 150\text{ }^\circ\text{C}$ and $230 \pm 10\text{ }^\circ\text{C}$ can be identified. In the medium-temperature region, the intensity of H_2 consumption increases with an increase in the nickel content. The peak is wide, without clearly defined maxima; its position slightly shifts towards higher temperatures with increasing x . In the high-temperature region, there is one peak, the maximum of which shifts from 880 to $780\text{ }^\circ\text{C}$ as x increases from 0 to 0.8 .

As shown by XRD, Raman spectroscopy, and TEM methods (Figures 6–9, Table 2), Ni^{2+} cations in $Ce_{1-x}Ni_xO_y$ are stabilized in a CeO_2 -based solid solution and fine NiO particles of $\sim 5\text{ nm}$ in size. The share of the latter increases with the growth of x and becomes significant only at $x \geq 0.7$. For comparison, Figure 10 also shows the TPR data for samples where Ni^{2+} ions are stabilized only in the form of well-crystallized NiO particles with an average size of $\sim 50\text{ nm}$. The first sample is a sample with $x = 0.3$ obtained by the impregnation method and calcined at $500\text{ }^\circ\text{C}$; the second is a sample with $x = 0.2$ obtained by the polymerizable complex method and calcined at $900\text{ }^\circ\text{C}$. The reduction profiles of these samples are similar and are described by three hydrogen consumption regions with maxima at 230 , 350 , and $830\text{ }^\circ\text{C}$. The fraction of [Ni-Ce-O] structures in such non-dispersed samples is insignificant. Note also that, in the impregnated samples, with an increase in the Ni content, the intensity of H_2 consumption increases only in the medium-temperature region [30].

Based on the analysis of literature data [12,98–101] and the results of studying samples by structural methods, the H_2 consumption in the low-temperature region indicates the reduction of [Ni-O-Ce] structures localized on the surface of the solid solution or at the interface between fine NiO particles and CeO_2 crystallites:



where V is an oxygen vacancy.

The H_2 consumption in the medium-temperature region indicates the reduction of Ni^{2+} cations in the bulk of CeO_2 -based solid solution as well as NiO particles. The third region of hydrogen uptake is associated with the reduction of Ce^{4+} cations localized in the volume of particles. This process becomes easier as x increases. Samples of the $Ce_{1-x}Ni_xO_y$ -series are characterized by close values of the specific surface area (Table 1) and, as a consequence, a comparable content of easily reduced surface [Ni-O-Ce] structures in their composition, regardless of the different nickel contents. This type of structure is the main one at $x \leq 0.1$. On the contrary, the fraction of the second type of Ni^{2+} increases with increasing x : for $x < 0.7$ it is mainly [Ni-O-Ce] structures in the bulk of CeO_2 -based solid solution, while at $x \geq 0.7$ the contribution of NiO particles grows. In any case, for M-free samples with a wide range of $x = 0.01$ – 0.8 , the reduction of Ni^{2+} ends at a temperature not higher than $500\text{ }^\circ\text{C}$.

The introduction of M into the composition of the samples greatly changes their reducing properties (Figure 10b). For $(CeM)_{1-x}Ni_xO_y$ with $M = Al$ or La , the profile of the TPR curve is similar to that of the sample without M , but it is shifted to the high-temperature region ($\Delta T = 100$ – $200\text{ }^\circ\text{C}$). Considering the structural data (Table 2), this is mainly due to the reduction of Ni^{2+} cations in the [Ni-O-Ce] and [Ni-O-M] structures of the surface and the bulk CeO_2 -based solid solution. For $(CeMg)_{1-x}Ni_xO_y$, the profile is different. In this case, the intensity of H_2 consumption significantly decreases and it appears in the regions 150 – $350\text{ }^\circ\text{C}$ and 500 – $700\text{ }^\circ\text{C}$. Taking into account the phase composition of Mg-containing samples (Table 2), it can be assumed that in the low-temperature region, surface and bulk [Ni-O-Ce] structures are reduced, while in the high-temperature region, NiO-MgO solid solution undergoes reduction [102]. Therefore, the feature of $(CeM)_{1-x}Ni_xO_y$ ($M = Al$,

La, and Mg) series is that a significant part of the Ni^{2+} is reduced at $T = 500\text{--}700\text{ }^\circ\text{C}$. This trend increases with increasing M/Ce molar ratio and for Mg-containing samples. An increase in the Ni^{2+} reduction temperature for $(\text{CeM})_{1-x}\text{Ni}_x\text{O}_y$ indicates the increasing strength of the metal–support interaction [23]. For $(\text{CeM})_{1-x}\text{Ni}_x\text{O}_y$ (M = Al, La) samples with a high M/Ce molar ratio, the idea that the formation of joint highly dispersed surface Al–Ni–O or La–Ni–O structures was reduced in the high-temperature region cannot be ruled out [60,103].

Total hydrogen consumption for $(\text{CeM})_{1-x}\text{Ni}_x\text{O}_y$ samples during TPR increases with increasing x , which is associated with an increase in the Ni content, and in the series Mg→Al→La, which indicates an increase in the reducibility of samples (Figure 11). The lower hydrogen uptake of the Mg-containing system may be due to the presence of a hard-to-reduce NiO–MgO solid solution.

Figure 12 shows in situ XRD data for the reduction of $(\text{CeM})_{1-x}\text{Ni}_x\text{O}_y$ samples in a 30% $\text{H}_2/70\%$ He mixture as a function of temperature. When the samples are reduced, the CeO_2 -based phase is retained, and the formation of metallic Ni is observed. For M-free samples, traces of Ni^0 phase are observed at $500\text{ }^\circ\text{C}$ (Figure 12a) which corresponds to the temperature of full reduction of Ni^{2+} cations according TPR data (Figure 10a). This correlates with the data that Ni exsolution, atomic diffusion of Ni toward the surface, and the nucleation of Ni particles start and proceed at lower temperatures than anticipated from their appearance in the crystallized phase in XRD [104]. For $(\text{CeM})_{0.8}\text{Ni}_{0.2}\text{O}_y$ (M = Al, La, Mg) the temperature of the formation of the metallic nickel phase depends upon the type of M. The temperature at which reflections of metallic nickel in the diffraction pattern clearly appear, increases from 500 to $650\text{ }^\circ\text{C}$ in the series Mg→Al→La (Figure 12). For Al and La-containing samples at this temperature ($T > 600\text{ }^\circ\text{C}$), the reduction of Ni^{2+} cations is practically completed (Figure 10b). For the Mg series, on the contrary, at $T = 500\text{ }^\circ\text{C}$, only a part of the Ni^{2+} cations is reduced—in the composition of the [Ni–Ce–O] structures. Nickel cations in the composition of NiO–MgO are reduced in a higher temperature region (Figure 10b). Additionally, for the Al-containing system, a peak at $2\theta = 26.4^\circ$ was observed during reduction, which can be attributed to the oxygen-deficient CeO_y phase. Its low intensity indicates a small amount of this phase.

The evolution of the unit cell volume of a CeO_2 -based solid solution during reduction exhibits a complex pattern (Figure 13). With thermal treatment, thermal expansion of the lattice is expected, while a sudden change in the slope may be associated with a chemical process [36,70,81,105]. Indeed, for the $(\text{CeM})_{1-x}\text{Ni}_x\text{O}_y$ samples, there is a region where the expected growth of the unit cell volume due to thermal expansion does not occur. Note that this behavior is typical only for Ni-containing samples. For nickel-free oxides (dot lines in Figure 13), a continuous increase in the unit cell volume with increasing temperature is observed. The studied temperature range (up to $700\text{ }^\circ\text{C}$) is insufficient for the reduction of Ce^{4+} cations in the volume of crystallites. Therefore, the decrease in the lattice expansion rate may be associated with a change in the lattice composition due to Ni^{2+} exsolution from CeO_2 and the complicated activities of vacancies formed according to reaction (12) during the reduction process. The mobility of oxygen vacancies, their dimerization, clustering, or migration from the lattice to the surface to fill low-energy spaces, affects the structural parameters of samples [106].

With the exception of the Al-containing sample, the size of crystallites of CeO_2 -based solid solution increases during the thermal treatment in H_2 (Figure 13). The degree of crystallite growth is higher for the M-free sample ($6.2 \rightarrow 21.3\text{ nm}$) and increases in the series M La ($4.4 \rightarrow 7.8\text{ nm}$) < Mg ($3.6 \rightarrow 11.2\text{ nm}$). For an Al-containing sample, the size of solid solution crystallites remains at the level of $2\text{--}3\text{ nm}$. Accordingly, the introduction of M into the composition of the samples effectively prevents sintering. This effect increases in the series Mg→La→Al.

The XRD data for $(\text{CeM})_{1-x}\text{Ni}_x\text{O}_y$ samples after activation at $800\text{ }^\circ\text{C}$ for 1 h in a 30% $\text{H}_2/70\%$ Ar flow is presented in Table 3 and Figure 14.

Table 3. Phase composition and structural properties of $(\text{CeM})_{1-x}\text{Ni}_x\text{O}_y$ samples after activation.

Sample	Textural Characteristics			XRD Data		
	$S_{\text{BET}}, \text{m}^2/\text{g}$	$V_p, \text{cm}^3/\text{g}$	D_p, nm	Phase Composition	a, nm	CSR, nm
Unmodified CeO₂						
CeO ₂	7	0.07	39.4	CeO ₂	0.5414	50.0
Without M						
Ce _{0.99} Ni _{0.01} O _{1.99}	13	0.08	26.5	CeO ₂	0.5415	50.0
Ce _{0.95} Ni _{0.05} O _{1.95}	21	0.06	11.0	CeO ₂	0.5419	25.0
Ce _{0.9} Ni _{0.1} O _{1.9}	21	0.08	14.7	CeO ₂	0.5419	25.0
				Ni		8.5
Ce _{0.8} Ni _{0.2} O _{1.8}	20	0.07	15.0	CeO ₂	0.5419	25.0
				Ni		15.0
Ce _{0.7} Ni _{0.3} O _{1.7}	28	0.15	21.7	CeO ₂	0.5419	50.0
				Ni		50.0
Ce _{0.3} Ni _{0.7} O _{1.3}				CeO ₂	0.5426	50.0
				Ni		50.0
Ce _{0.2} Ni _{0.8} O _{1.2}	4	0.05	50.0	CeO ₂	0.5426	50.0
				Ni		50.0
M = Al						
Ce _{0.6} Al _{0.2} Ni _{0.2} O _{1.7}	23	0.14	24.8	CeO ₂	0.5424	6.5
				Ni		6.0
Ce _{0.4} Al _{0.4} Ni _{0.2} O _{1.6}	11	0.15	55.0	CeAlO ₃		
				Ni		15.0
Ce _{0.2} Al _{0.7} Ni _{0.1} O _{1.5}	10	0.04	15.8	X-ray amorphous phase	–	–
Al _{0.9} Ni _{0.1} O _{1.5}				X-ray amorphous phase	–	–
M = La						
Ce _{0.6} La _{0.2} Ni _{0.2} O _{1.7}	10	0.11	44.1	CeO ₂	0.5490	25.0
				Ni		15.0
Ce _{0.4} La _{0.4} Ni _{0.2} O _{1.6}	17	0.14	32.7	CeO ₂	0.5600	22.0
				Ni		12.0
Ce _{0.2} La _{0.6} Ni _{0.2} O _{1.5}	20	0.25	50.6	La(OH) ₃	–	–
La _{0.8} Ni _{0.2} O _{1.4}	29	0.23	30.9	La(OH) ₃	–	–
M = Mg						
Ce _{0.6} Mg _{0.2} Ni _{0.2} O _{1.6}	12	0.16	53.1	CeO ₂	0.5420	50.0
				MgO (traces)		
				Ni		12.0
Ce _{0.4} Mg _{0.4} Ni _{0.2} O _{1.4}	12	0.10	25.8	CeO ₂	0.5425	22.0
				MgO	0.4222	12.0
				Ni		12.0
Ce _{0.2} Mg _{0.7} Ni _{0.1} O _{1.2}	30	0.26	34.0	CeO ₂	0.5417	12.5
				MgO	0.4221	12.5
				Ni		15.0
Mg _{0.9} Ni _{0.1} O	51	0.33	26.6	MgO	0.4221	19.5

It can be seen that the activated samples of the $\text{Ce}_{1-x}\text{Ni}_x\text{O}_y$ -series contain a CeO₂-based phase and the phase of metallic nickel. For the CeO₂-based phase, an increase in the unit cell parameter (Δa is equal to 0.0006 \rightarrow 0.0019 at $x = 0.1 \rightarrow 0.8$) is observed, which may indicate the release of nickel cations from the structure as well as an increase in the Ce³⁺/Ce⁴⁺ molar ratio. The average size of ceria crystallites amounts to 25–50 nm, which is significantly higher than in fresh samples. The average size of the formed Ni⁰ crystallites depends on the nickel content and increases from 8.5 to 50 nm with increasing x from 0.1 to 0.8.

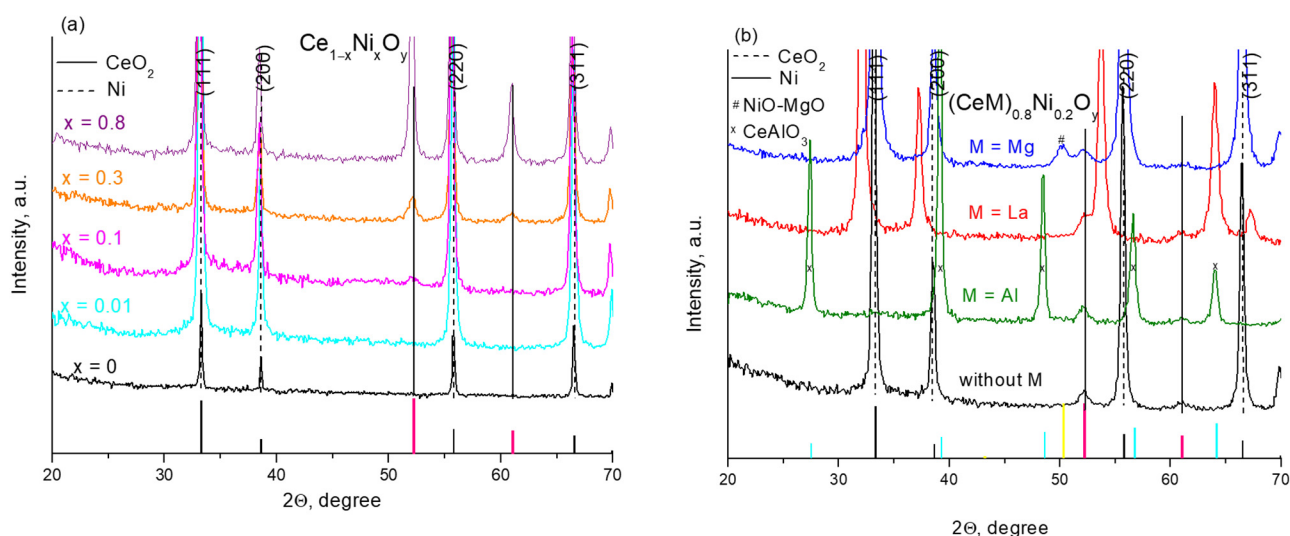


Figure 14. XRD patterns for $(\text{CeM})_{1-x}\text{Ni}_x\text{O}_y$ ($M = \text{Al, La, Mg}$) samples after activation: effect of Ni molar fraction (a) and M type (b). (b) M/Ce molar ratio is equal to 1. The standard patterns of CeO_2 (ICDD 43–1002, black bars), Ni (ICDD 04–0850, pink bars), MgO (ICDD 45–0946, magenta bars), and CeAlO_3 (ICDD 28–0260 cyan bars) are shown.

Phase and structural transformations of $(\text{CeM})_{1-x}\text{Ni}_x\text{O}_y$ samples as a result of reduction are more complex and depend on the type of M and the M/Ce molar ratio. In the case of $M = \text{Al}$, after activation, the CeO_2 -based solid solution is retained only at $\text{Al/Ce} = 0.3$. For a sample with $\text{Al/Ce} = 1$, it transforms into the CeAlO_3 phase. The size of nickel crystallites in these samples is 6–15 nm. At higher Al/Ce molar ratios, the samples have an X-ray amorphous structure (Table 3). In the case of $M = \text{La}$, at $\text{La/Ce} \leq 3$, the samples after activation contain a CeO_2 -based phase and the phase of metallic nickel. A high cell parameter indicates the existence of the Ce-La-O-solid solution after Ni exsolution. At higher La/Ce , the CeO_2 -based solid solution disintegrates as a result of the sample activation with the formation of lanthanum hydroxide (Table 3). Ce- and Ni-containing components are present in X-ray amorphous forms. For $M = \text{Mg}$, the changes resulting from activation are similar to those found for the M-free series. A distinguishing feature of this series is the presence of the magnesium oxide phase with an average crystallite size of 12 nm. Note that the lattice parameter of this phase indicates that the selected activation conditions ensure the reduction of the NiO-MgO solid solution present in the fresh sample. The absence of the Ni^0 -phase reflections in the XRD patterns of the samples with $M/\text{Ce} > 1$ ($M = \text{Al}$ or La) after activation indicates its high dispersion.

Additional information about sample transformation during activation is provided by HRTEM, EDX mapping (Figure 15), and SEM (Figure 16). On the surface of the $(\text{CeM})_{1-x}\text{Ni}_x\text{O}_y$ samples, Ni species of two types are observed: nanocrystallites of 2–4 nm in size and nanoparticles of 8–15 nm in size. Larger particles have a core-shell structure; their surface is covered with a layer of NiO oxide after contact with air. Most likely the most-dispersed crystallites are also oxidized on the surface or completely upon contact with air but are easily reduced by the electron beam in the microscope. EDX mapping shows that in cases of $M = \text{Al}$ or La , the homogeneous distribution of Ce and M is retained after Ni exsolution. This correlates with the XRD data, pointing to the existence of a Ce-M-O phase in the sample after activation. For $M = \text{Mg}$, the co-existing CeO_2 and MgO phases are observed, which indicates full destruction of the CeO_2 -based solid solution along with Ni exsolution upon the sample activation.

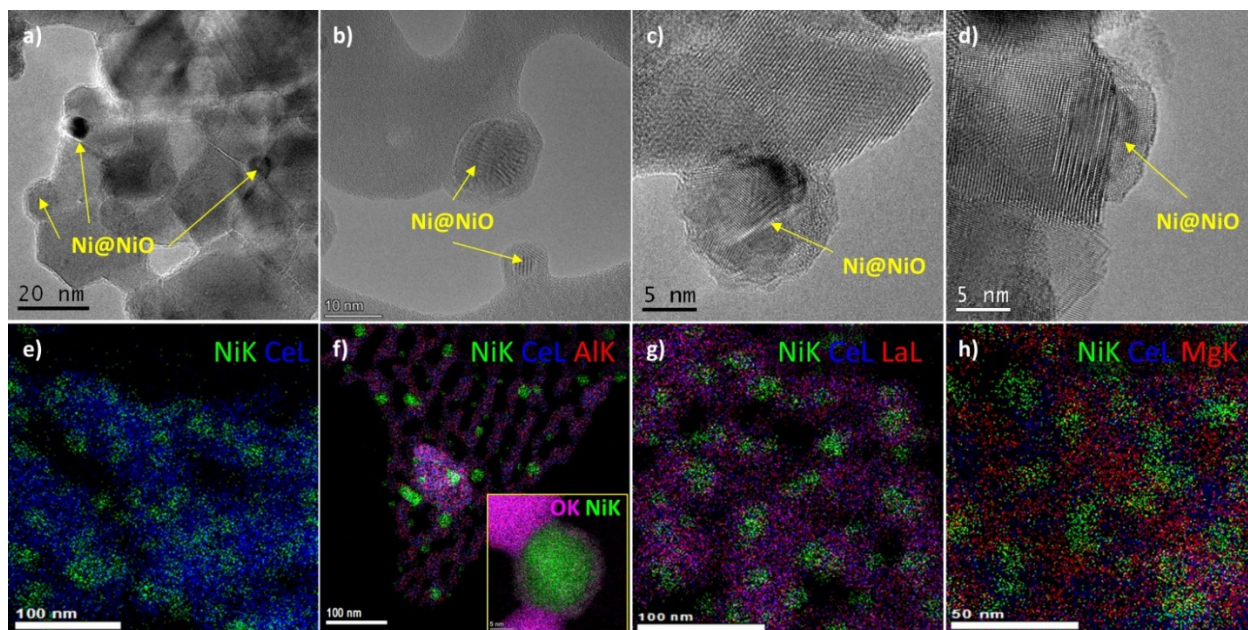


Figure 15. HRTEM pictures (a–d) and EDX mapping (f–h) of $\text{Ce}_{0.8}\text{Ni}_{0.2}\text{O}_y$ (a,e) and $(\text{CeM})_{0.8}\text{Ni}_{0.2}\text{O}_y$ (M = Al (b,f)), La (c,g), Mg (d,h) samples. M/Ce molar ratio is equal to 1.

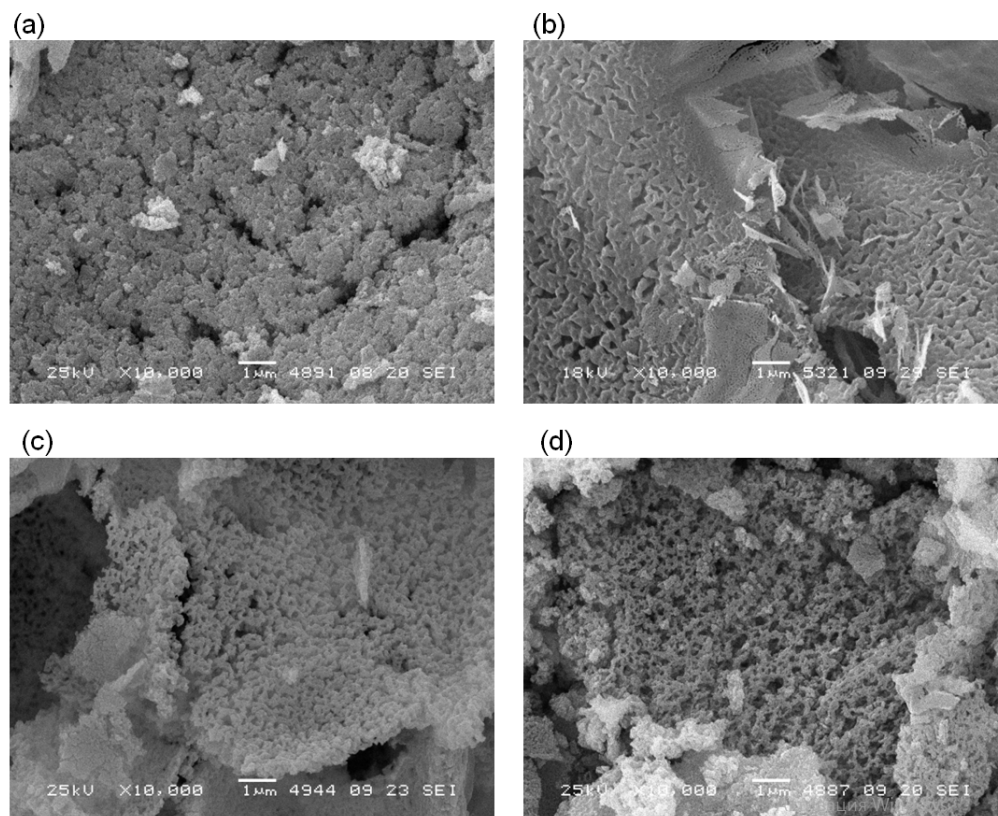


Figure 16. SEM images of $(\text{CeM})_{0.8}\text{Ni}_{0.2}\text{O}_y$ samples after activation: without M (a), M = Al (b), La (c), and Mg (d). (b–d) M/Ce molar ratio is equal to 1.

After activation, the samples retained a spongy morphology (Figure 16) and mesoporosity. The average diameter of pores is within the wide range of 11–55 nm (Table 3). Nonetheless, the specific surface area of $(\text{CeM})_{1-x}\text{Ni}_x\text{O}_y$ samples decreases as a result of high-temperature treatment during activation. To a lesser extent, S_{BET} declines in samples with an initially lower surface. For example, at $M/\text{Ce} = 1$, S_{BET} decreases by factors of 7.2 ($80 \rightarrow 11 \text{ m}^2/\text{g}$), 2.8 ($48 \rightarrow 17 \text{ m}^2/\text{g}$), and 2.4 ($36 \rightarrow 15 \text{ m}^2/\text{g}$) for $M = \text{Al}$, La and $M = \text{Mg}$, respectively. Differences in the textural properties of the samples become less noticeable. Generally, all values of the specific surface area of activated $(\text{CeM})_{0.8}\text{Ni}_{0.2}\text{O}_y$ samples are within the range of $20 \pm 10 \text{ m}^2/\text{g}$ (Table 3). Only for $x \geq 0.7$ S_{BET} decreases to $\sim 5 \text{ m}^2/\text{g}$.

Thus, in the $(\text{CeM})_{1-x}\text{Ni}_x\text{O}_y$ samples, as a result of activation, exsolution from fluorite structure and reduction of Ni^{2+} cations occur, and Ni^0 particles are formed. The temperature range of Ni^0 phase formation is higher for samples with a higher Ni content and increases with an increase in the molar ratio M/Ce and in the series $M\text{-free} < \text{Al} = \text{La} < \text{Mg}$. This indicates an increase in the Ni–support interaction upon the introduction of M into the sample. In the case of $M = \text{Al}$ or La , the oxide matrix is the Ce-M-O joint phase, which is in contact with Ni^0 nanoparticles. The situation is opposite in the case of $M = \text{Mg}$: there are coexisting CeO_2 , MgO , and Ni^0 phases. In situ XRD study in the temperature range up to $700 \text{ }^\circ\text{C}$ shows that the resistance to sintering of the CeO_2 -based phase is higher in the case of doping $M = \text{Al}$ or La , i.e., when a CeO_2 -based solid solution continues to exist after activation. After activation at $800 \text{ }^\circ\text{C}$, the dispersion of the Ni^0 phase at the same content is comparable at $M/\text{Ce} \leq 1$ for all studied M . There are two types of species: nanocrystallites (2–4 nm) and nanoparticles with an average size of 12–15 nm ($x = 0.2$). This is a fairly low nickel particle size at its content of 10 wt.%. For comparison, at the same Ni content and temperature of reduction, the Ni^0 crystallite size varies from 19 to 33 nm for impregnated $10\text{Ni}/\text{CeO}_2$ samples [71,105] and from 20 to 46 nm for $10\text{Ni}/\text{CeO}_2$, prepared using the hydrothermal method [36]. As x increases from 0.1 to 0.8, the average particle size increases from 8 to 50 nm. At higher M/Ce molar ratio, the influence M becomes stronger. At $M/\text{Ce} > 1$, in contrast to Mg , the presence of Al or La in the composition of $(\text{CeM})_{1-x}\text{Ni}_x\text{O}_y$ samples ensures a higher dispersion of the Ni^0 phase as a result of activation. Thus, the activated $(\text{CeM})_{1-x}\text{Ni}_x\text{O}_y$ samples have similar textural and morphological properties but different structural characteristics and resistance to sintering due to the different strength of Ni–support interaction, which can affect their functional performance.

2.3. Functional Properties

The functional properties (activity, stability, and anti-coking ability) of the $(\text{CeM})_{1-x}\text{Ni}_x\text{O}_y$ samples were studied in the methane bi-reforming reaction when tested in screening and stability modes.

Figure 17 shows the temperature dependences of product concentrations during the bi-reforming of methane over $(\text{CeM})_{1-x}\text{Ni}_x\text{O}_y$ samples. In the case of $x = 0.05$ (Figure 17a), the CH_4 and CO_2 conversion starts at $600 \text{ }^\circ\text{C}$, but the quantity of reforming products— CO and H_2 —is negligible ($<10 \text{ vol.}\%$). As the temperature rises, concentrations of methane and carbon dioxide decrease, while those of CO and hydrogen increase. This tendency is more pronounced for samples with $x \geq 0.2$ (Figure 17b–e), for which higher values of H_2 and CO concentrations are achieved in the whole temperature range $600\text{--}850 \text{ }^\circ\text{C}$. In the case of $M = \text{Al}$ or Mg , the process parameters at $850 \text{ }^\circ\text{C}$ are close to thermodynamic equilibrium results (Figure 17f).

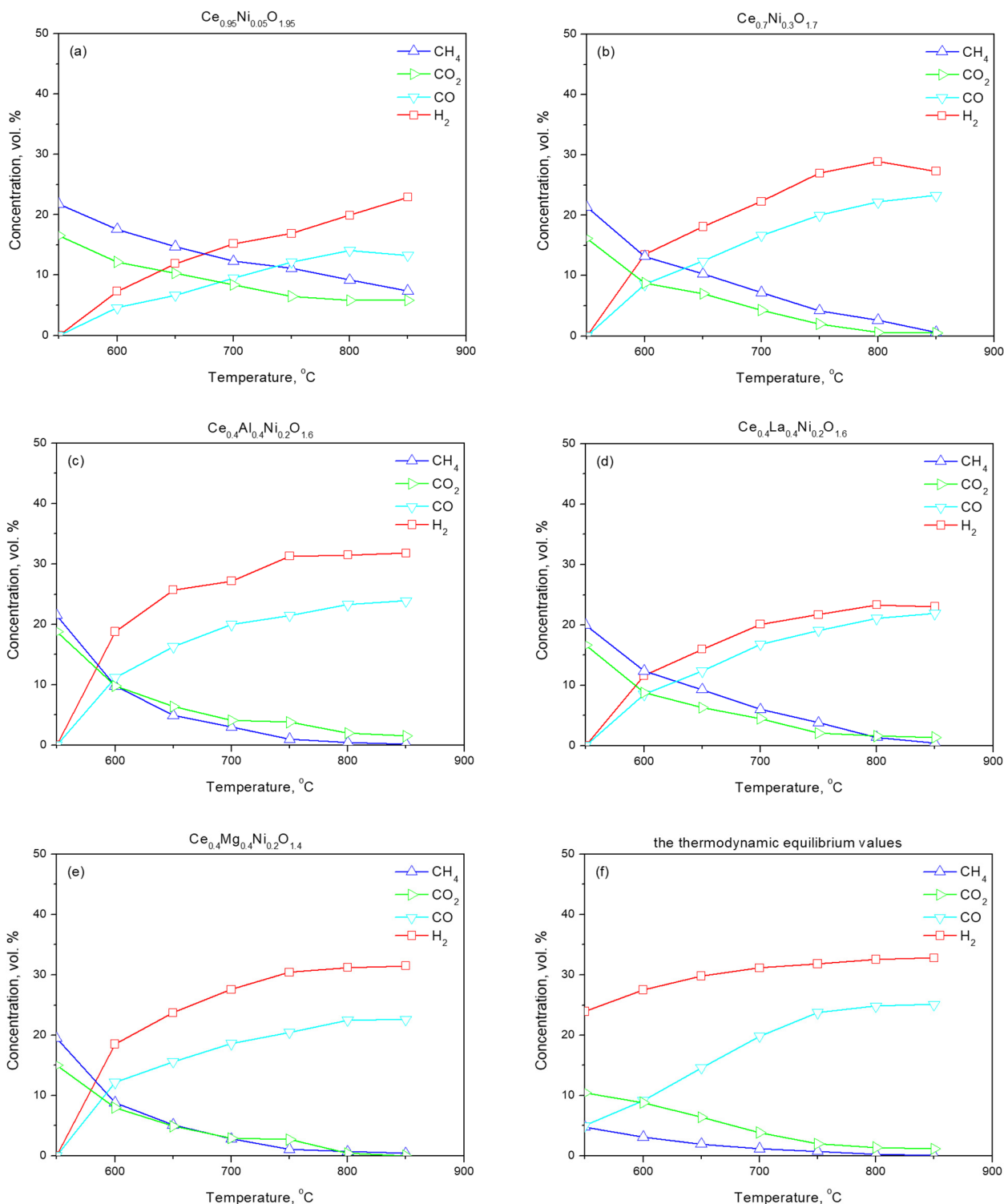


Figure 17. Temperature dependence of reagent and product concentrations during the bi-reforming of methane over $Ce_{1-x}Ni_xO_y$ (a,b) and $(CeM)_{0.8}Ni_{0.2}O_y$ (c–e) samples and the thermodynamic equilibrium values (f). (a) $x = 0.05$; (b) $x = 0.3$; (c–e) M/Ce molar ratio is equal to 1, $M = Al$ (c), La (d), and Mg (e).

The parameters of the bi-reforming of methane over $(\text{CeM})_{1-x}\text{Ni}_x\text{O}_y$ samples depend on the values of x (Figure 18) and type of M (Figure 19). It was found that with an increase in x from 0.05 to 0.8, both the conversion of reactants and the yield of products increased, reaching the following values at 750 °C: $X(\text{CH}_4)$ 32 → 86%, $X(\text{CO}_2)$ 46 → 73%, $Y(\text{H}_2)$ 45 → 92%, and $Y(\text{CO})$ 43 → 85%. Catalyst productivity also grew with increasing x : from 8.1 to 12.0 $\text{L}(\text{H}_2)/(\text{g}_{\text{cat}}\cdot\text{h})$ which may be connected with a higher content of Ni and, accordingly, a higher content of active Ni species per gram of catalyst. However, the efficiency of H_2 formation per mole of Ni decreases from 17.7 to 1.1 $\text{mole}_{\text{H}_2}/(\text{mole}_{\text{Ni}}\cdot\text{min})$ (Figure 18b). It can be seen that, in contrast to the conversion and yield indicators, the specific indicator (calculated per mole of the Ni active component) of the catalyst activity decreases with an increase in x . This may be due to an increase in the average particle size of the Ni active component (8 → 50 nm, Table 3), and, accordingly, a decrease in the fraction of available surface-active sites. The surface atoms/bulk atoms ratio rapidly decreases with increasing particle size: at a particle size of 3 nm, 50% of atoms or ions are on the surface, while at a size of 10 nm it is ~15% and at a size of 25 nm it is ~5% [107]. It can be concluded that at $x = 0.2$, a compromise is reached between sufficiently high catalyst productivity and a not-quite-low specific rate of hydrogen formation.

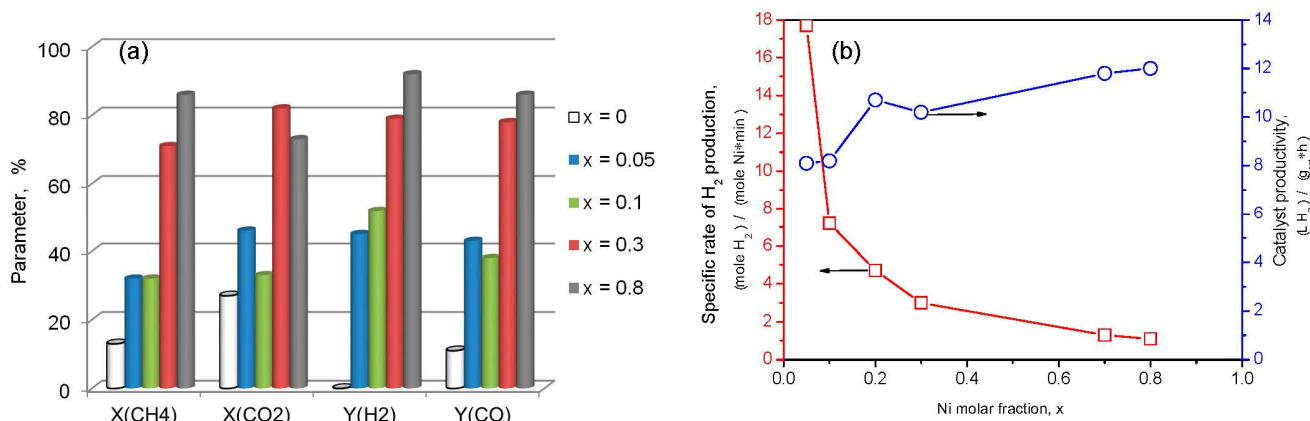


Figure 18. Effect of Ni molar fraction (x) on the parameters during the bi-reforming of methane at 750 °C (a), specific rate of H_2 production and catalyst productivity at 850 °C (b) over $\text{Ce}_{1-x}\text{Ni}_x\text{O}_y$ samples.

The performance of $(\text{CeM})_{0.8}\text{Ni}_{0.2}\text{O}_y$ in the bi-reforming of methane exceeds that of $\text{Ce}_{0.8}\text{Ni}_{0.2}\text{O}_{1.8}$ (Figure 19). An exception is the La-containing sample, in the presence of which, despite the high values of the conversion of the reagents, a reduced yield of hydrogen is observed. This may indicate the accumulation of carbonaceous deposits according to the reactions (8–9). Indeed, after screening tests (stepwise temperature-rise mode, 650 → 850 °C) the samples contain coke, the content of which increases in the series 0.8 wt.% ($M = \text{Al}$) \approx 0.9 wt.% ($M = \text{Mg}$) < 2.7 wt.% (M -free) < 6.9 wt.% ($M = \text{La}$). At constant type of M , changing the M/Ce ratio has little effect on catalyst performance in screening tests. There is a slight tendency to a decrease in the hydrogen yield with an increase in the M/Ce molar ratio.

Note that the activity in screening tests of the studied $(\text{CeM})_{0.8}\text{Ni}_{0.2}\text{O}_y$ samples, prepared using the PC method, is comparable with that of impregnated samples of the same composition [108], while the degree of coking is significantly lower (Figure 20). For both cases, the Mg-containing samples are the most resistant to coking.

Table 4 and Figure 21 demonstrate the effect of Ni molar fraction (x), type of M , molar ratio M/Ce , and preparation method on the parameters of the bi-reforming of methane at 800 °C during stability tests. A decrease in process performance over time is observed when M -free samples are used as catalysts or at $M = \text{La}$. The degree of sample deactivation, calculated as the relative decrease in H_2 yield over 24 h of time on stream, is at the maximum (35%) for a sample with a low Ni molar fraction ($x = 0.05$). For the La-series, it does not

exceed 10% (Table 4). On the contrary, in the case of $M = \text{Al}$ or Mg , the process values practically do not change with time on stream. As in the screening tests, in the stability tests, the M/Ce molar ratio has little effect on the activity of the samples. Among the studied types of M , the yield of hydrogen increases in the series $M\text{-free} < \text{La} < \text{Mg} < \text{Al}$ (Figure 21). Better performance of methane reforming is observed for samples obtained by the PC method rather than by impregnation (Figure 21d).

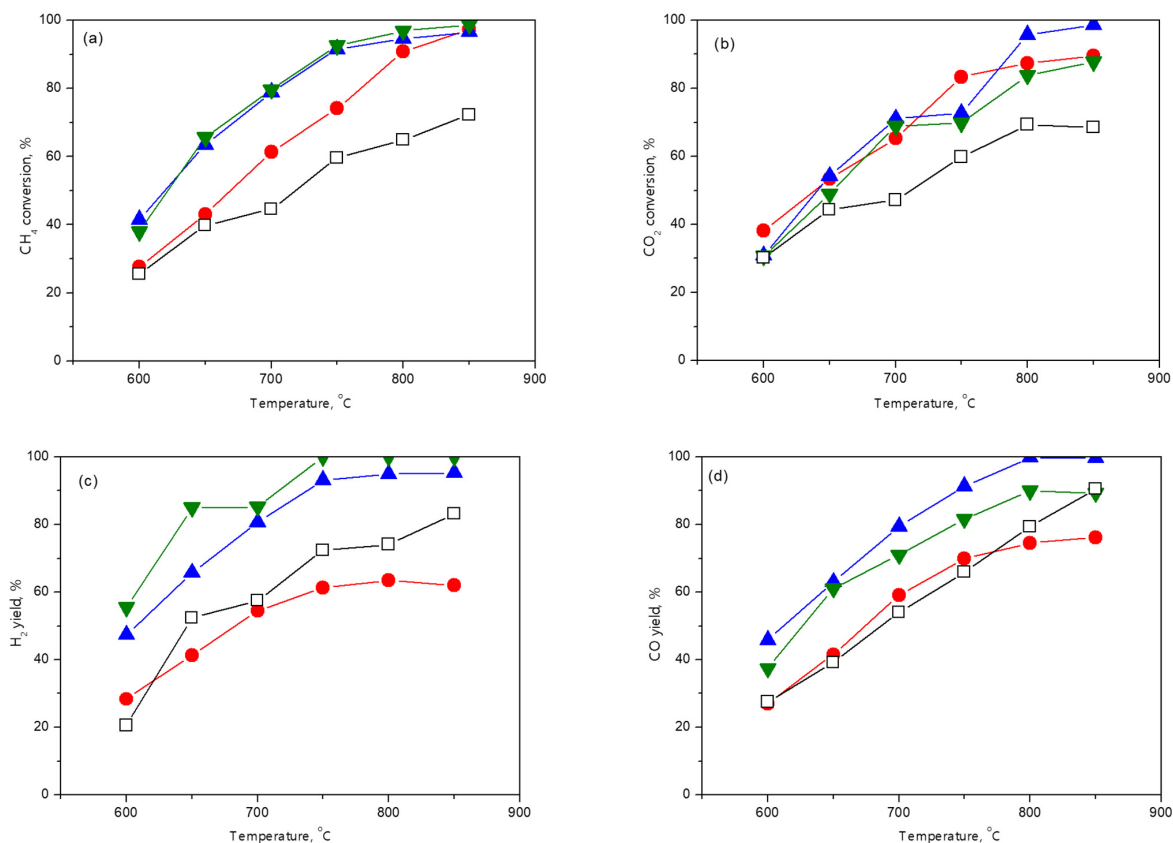


Figure 19. Temperature dependence of CH_4 conversion (a), CO_2 conversion (b), H_2 yield (c), and CO yield (d) during the bi-reforming of methane over $(\text{CeM})_{0.8}\text{Ni}_{0.2}\text{O}_y$ samples: effect of M type. M/Ce molar ratio is equal to 1. \square —without M ; \blacktriangledown — $M = \text{Al}$; \bullet — $M = \text{La}$; \blacktriangle — $M = \text{Mg}$.

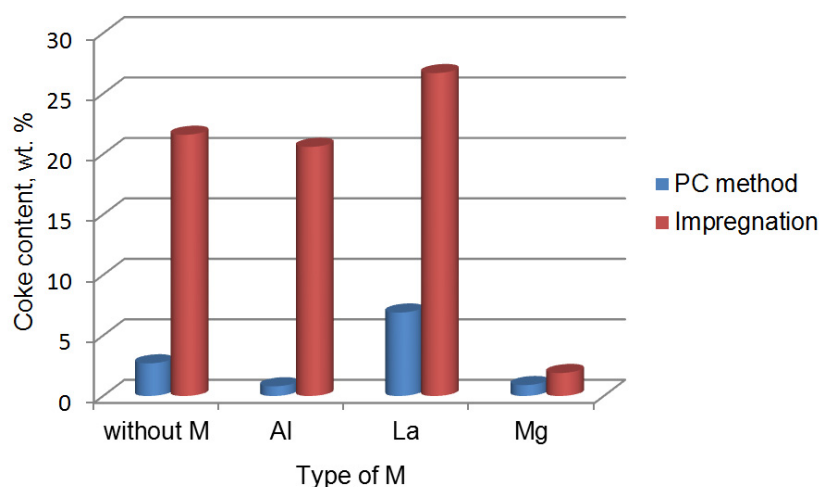


Figure 20. Effect of preparation method of $(\text{CeM})_{0.8}\text{Ni}_{0.2}\text{O}_y$ on the content of coke formed during screening tests of samples for the bi-reforming of methane. M/Ce molar ratio is equal to 1.

Table 4. Effect of Ni molar fraction (x), type of M, and molar ratio M/Ce on the parameters of the bi-reforming of methane at 800 °C over (CeM)_{1-x}Ni_xO_y samples.

Sample	Time on Stream, h	X _{CH₄}	X _{CO₂}	Y _{H₂}	Y _{CO}	H ₂ /CO	Degree of Deactivation *, %	Carbon Accumulation Rate, mgC/g _{cat} ·h
Ce _{0.95} Ni _{0.05} O _{1.95}	2	31	39	40	37	1.5	35	0
	24	19	31	26	25	1.4		
Ce _{0.9} Ni _{0.1} O _{1.9}	2	62	61	67	60	1.4	21	0
	24	48	48	53	49	1.5		
Ce _{0.8} Ni _{0.2} O _{1.8}	2	79	75	84	79	1.5	15	0
	24	67	66	72	67	1.5		
Ce _{0.7} Ni _{0.3} O _{1.7}	2	74	83	73	78	1.3	10	0.38
	24	68	67	75	70	1.4		
Ce _{0.6} Al _{0.2} Ni _{0.2} O _{1.6}	2	87	84	99	88	1.4	0	0.16
	24	93	89	99	91	1.4		
Ce _{0.6} La _{0.2} Ni _{0.2} O _{1.7}	2	92	94	92	90	1.4	5	0.46
	24	96	87	88	89	1.4		
Ce _{0.4} La _{0.4} Ni _{0.2} O _{1.6}	2	91	90	91	87	1.4	0	1.33
	24	94	89	95	88	1.5		
Ce _{0.2} La _{0.6} Ni _{0.2} O _{1.5}	2	92	89	83	85	1.4	0	1.71
	24	92	90	93	88	1.5		
La _{0.8} Ni _{0.2} O _{1.4}	2	93	86	99	89	1.5	10	3.79
	24	95	87	90	91	1.5		
Ce _{0.6} Mg _{0.2} Ni _{0.2} O _{1.6}	2	90	86	90	87	1.4	0	0.08
	24	90	85	94	89	1.5		
Ce _{0.2} Mg _{0.7} Ni _{0.1} O _{1.2}	2	70	74	80	77	1.3	0	0.21
	24	84	90	86	84	1.3		
Mg _{0.9} Ni _{0.1} O	2	89	93	89	92	1.3	0	0.38
	24	88	89	91	87	1.4		

* Relative decrease in hydrogen yield after 24 h of time on stream.

Studied samples of optimal composition provide high and stable conversion of methane ($X_{\text{CH}_4} \approx 90\%$) and CO_2 ($X_{\text{CO}_2} \approx 85\%$), as well as a high hydrogen yield ($Y_{\text{H}_2} > 90\%$) that is comparable to or better than the literature data for the bi-reforming of methane [109–114]. Namely, during the bi-reforming of methane at 800 °C over impregnated Ni/CeO₂ catalyst, X_{CH_4} is equal to 50% [109], at 800 °C over co-precipitated Ni/CeO₂ it is 80% [109], at 900 °C over Ni–Ce–Fe/Al₂O₃ it is 90% [110], at 800 °C over Ni/SBA-15 it is 70% [111], at 800 °C over Ni/MgAl₂O₄ it is 90% [112], at 800 °C over Ni/Ce_{0.6}Zr_{0.4}O₂ it is 60% [113], and at 700 °C over Ni/ZrO₂ it is 45–70%, depending on the type of ZrO₂ [114].

The study of spent catalysts by thermal analysis shows that an insignificant weight loss (0.2–0.4 wt.%) occurs in the low-temperature region ($T < 200$ °C) due to the desorption of water and volatile intermediate products (Figure 22). Further, at a temperature of 300–500 °C, the weight of the sample increases, which is associated with the oxidation of the Ni⁰ active component. The process is accompanied by an exothermic effect, the maximum of which shifts from 345 to 420 °C in the series Al < La < Mg < M-free. This indicates the decrease in Ni stability to re-oxidation in the presence of M, which correlates with improvement to the metal–support interaction. This effect is more pronounced for M = Al. There is weight loss in the region of 500–800 °C. The exception is M-free samples with $x < 0.3$, for which no change in weight is observed in the high-temperature region. The amounts of this weight loss vary from 0.2 to 9 wt.% and can be assigned to the oxidation of carbonaceous deposits. Higher weight values due to the burnout of carbon deposits are observed for samples with M = La. The carbon accumulation rate decreases with the decrease of the molar ratio of M/Ce and in the series La → Al → Mg. Among (CeMg)_{0.8}Ni_{0.2}O_y samples, the minimum rate of formation of carbonaceous deposits was observed for the Ce_{0.6}Mg_{0.2}Ni_{0.2}O_{1.6} sample (Table 4). It is equal to 0.08 mgC/g_{cat}·h, which

is significantly lower than the specific rate of H₂ formation: 6.8×10^{-5} mole_C/(mole_{Ni}·min) vs. 5.0 mole_{H₂}/(mole_{Ni}·min).

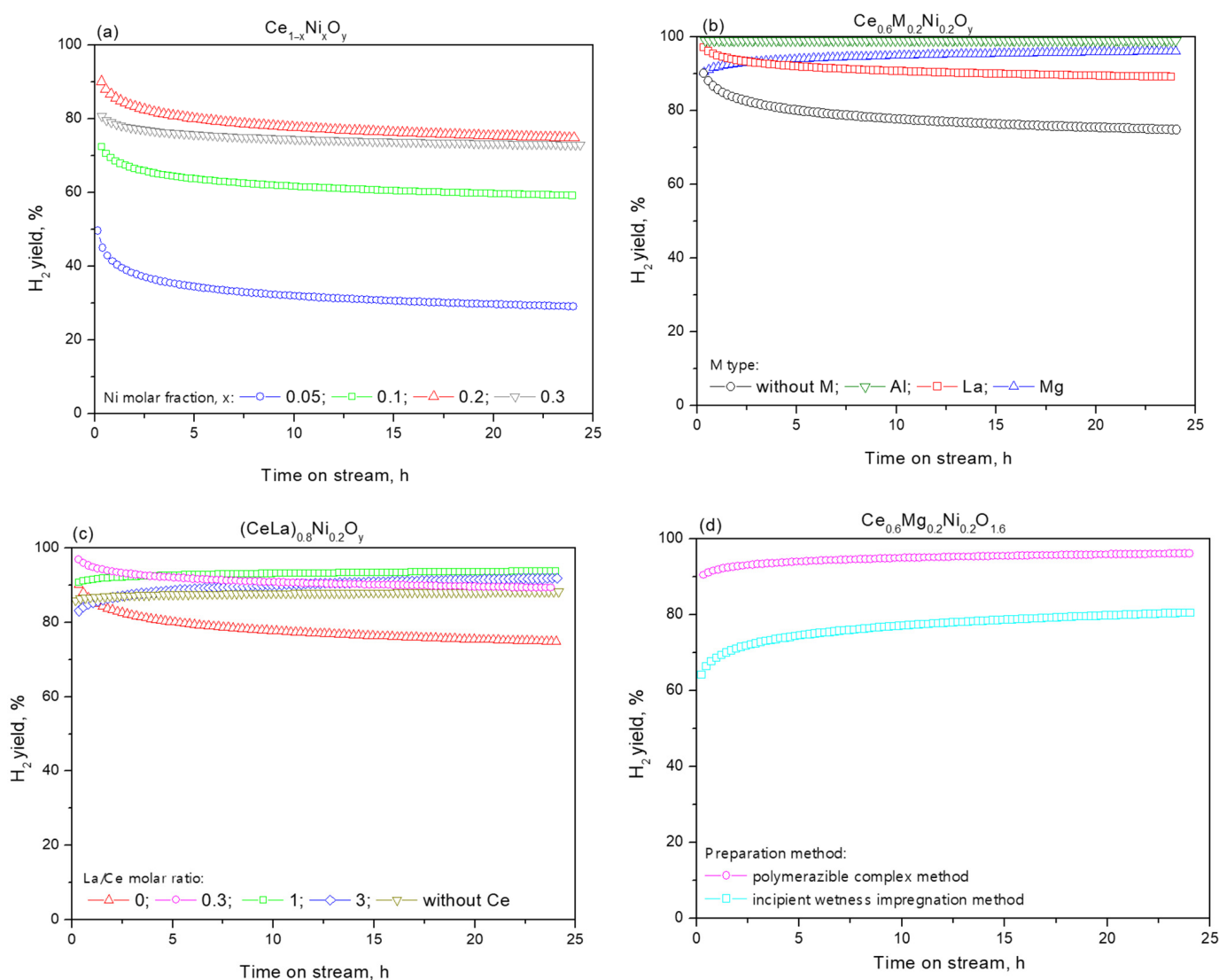


Figure 21. Effect of Ni molar fraction (a), type of M (b), molar ratio La/Ce (c) and preparation method (d) of the parameters of the bi-reforming of methane at 800 °C over (CeM)_{1-x}Ni_xO_y samples.

The main pathways of carbon formation are cracking (6) and Boudouard reaction (7). According to thermodynamic data, the selectivity of coke formation during the bi-reforming of methane decreases with increasing temperature [21]. Therefore, carbon formation occurs more intensively in screening tests than in stability tests: 6.9 vs. 3.2 and 0.9 vs. 0.4 wt.% for M = La and Mg and at M/Ce = 1. In comparison to the literature data, the carbon formation level for spent samples with M = Al or Mg is low. For example, after the bi-reforming of methane, 12% Ni/Al₂O₃ catalyst includes 50 wt.% of carbonaceous deposits (C) [110], 12% Ni–5% Ce–5% Fe/Al₂O₃–2 wt.% of C [110], 5% Ni/MgAl₂O₄–3 wt.% of C [112], 10% Ni/SBA-15–6.4 and 3% B-10% Ni/SBA-15–1.5 wt.% of C [111], for 10% Ni/ZrO₂ the content of C varies from 0.2 to 47.9 wt.% for different types of ZrO₂ support [114]. Therefore, a significant advantage of the developed materials is their high resistance to coking even when a low steam/CO₂ molar ratio (H₂O/CO₂ = 0.5) is used in the initial reaction mixture. This stability of the catalyst to coking may be due to several factors. First, this is connected with the anti-coking properties of ceria support [49,115], and second, the large size of Ni crystallites, on which, as was shown in [36], the coking rate is lower than for nickel particles

with a size of 20–30 nm. In addition to the influence of M on the rate of coke formation, its influence on the mode of change in the textural and structural properties of the samples $(\text{CeM})_{1-x}\text{Ni}_x\text{O}_y$ as a result of the reaction is expected.

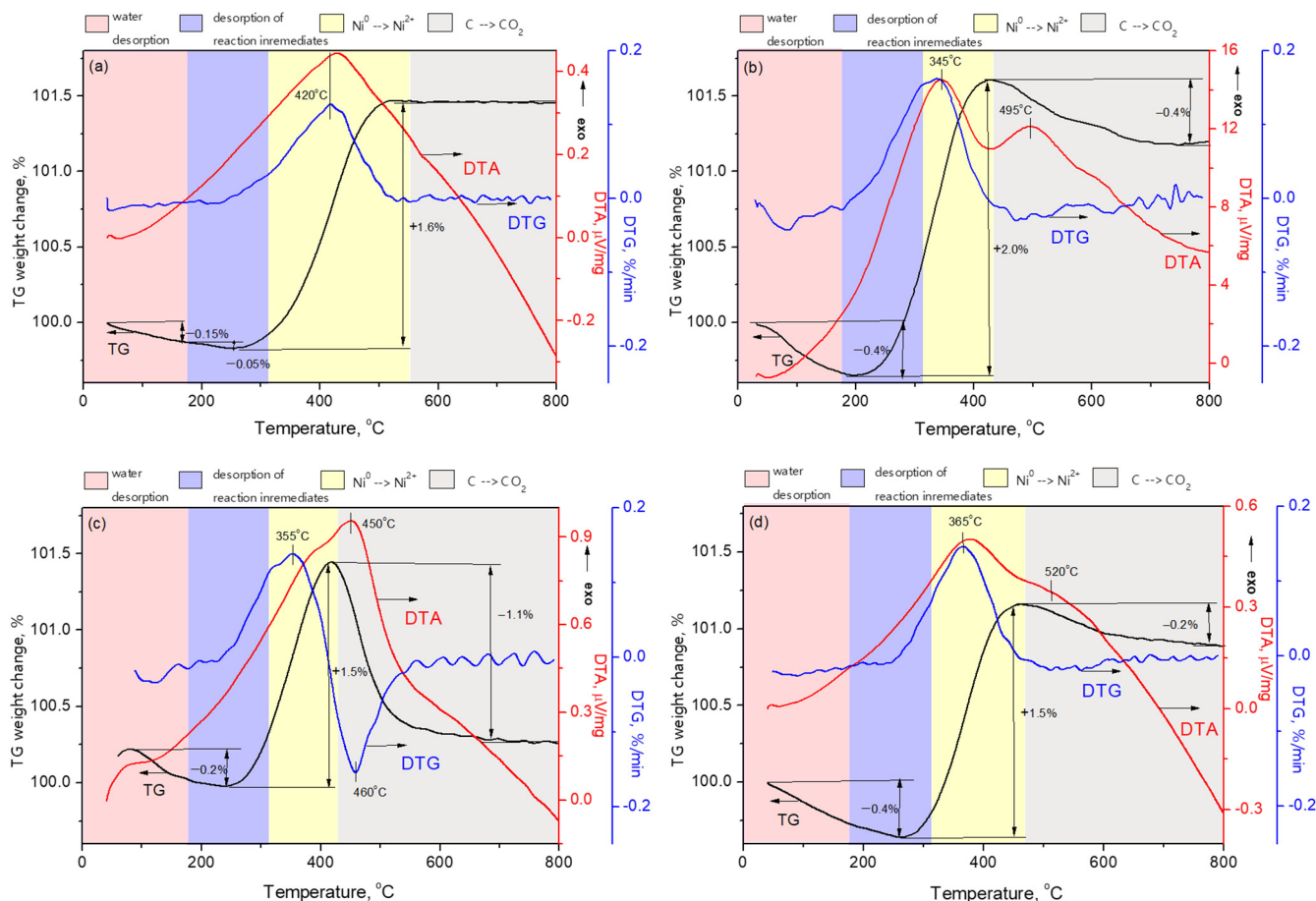


Figure 22. Thermal analysis of the spent $\text{Ce}_{0.8}\text{Ni}_{0.2}\text{O}_{1.8}$ (a) and $(\text{CeM})_{0.8}\text{Ni}_{0.2}\text{O}_y$ [M = Al (b), La (c), Mg (d)] sample in an air flow. (b–d) M/Ce molar ratio is equal to 0.3. Reaction conditions: 800 °C, 24 h.

2.4. Characterization of Spent Samples

The harsh conditions of the catalytic reaction (high temperatures, presence of water vapor, etc.) inevitably affect the properties of the samples. Table 5 presents the textural properties and phase composition of spent $(\text{CeM})_{1-x}\text{Ni}_x\text{O}_y$ samples.

The specific surface area of $\text{Ce}_{1-x}\text{Ni}_x\text{O}_y$ samples decreases from 20 to 5 m^2/g , while for the $(\text{CeM})_{1-x}\text{Ni}_x\text{O}_y$ samples it remains at the level of the values for the samples after activation ($15 \pm 5 \text{ m}^2/\text{g}$). This indicates a positive effect of M on the textural properties of the samples and a lower rate of thermal sintering of $(\text{CeM})_{1-x}\text{Ni}_x\text{O}_y$ samples. Spent samples lose the porous spongy structure that was observed for fresh (Figure 5) and activated (Figure 16) samples and consist of large aggregates of irregularly shaped particles (Figure 23). The morphology of the spent M-free sample looked particularly dense. The average pore diameter increases, reaching 20–50 nm in size (Table 5).

Table 5. Textural properties and phase composition of spent $(\text{CeM})_{1-x}\text{Ni}_x\text{O}_y$ samples.

Sample	Textural Properties			Phase Composition *
	S_{BET} , m^2/g	V_p , cm^3/g	D_p , nm	
Without M				
$\text{Ce}_{0.95}\text{Ni}_{0.05}\text{O}_{1.95}$	3	0.02	29.9	CeO_2 (50 nm, 0.5414 nm) ** Ni (50 nm)
$\text{Ce}_{0.9}\text{Ni}_{0.1}\text{O}_{1.9}$	4	0.03	34.8	CeO_2 (50 nm, 0.5411 nm) Ni (50 nm)
$\text{Ce}_{0.8}\text{Ni}_{0.2}\text{O}_{1.8}$	3	0.02	23.6	CeO_2 (50 nm, 0.5418 nm) Ni (50 nm)
$\text{Ce}_{0.7}\text{Ni}_{0.3}\text{O}_{1.7}$	5	0.03	23.9	CeO_2 (50 nm, 0.5418 nm) Ni (50 nm)
M = Al				
$\text{Ce}_{0.6}\text{Al}_{0.2}\text{Ni}_{0.2}\text{O}_{1.7}$	11	0.14	51.9	CeO_2 (12.0 nm, 0.5415 nm) Ni (25.0 nm)
$\text{Ce}_{0.4}\text{Al}_{0.4}\text{Ni}_{0.2}\text{O}_{1.6}$	10	0.13	51.4	CeAlO_3 Ni (21.0 nm)
$\text{Ce}_{0.2}\text{Al}_{0.7}\text{Ni}_{0.1}\text{O}_{1.5}$	8	0.09	44.5	X-ray amorphous phase Ni (8.0 nm)
$\text{Al}_{0.9}\text{Ni}_{0.1}\text{O}_{1.5}$	21	0.12	22.5	Al-Ni-O (-, 0.8000 nm) Ni
M = La				
$\text{Ce}_{0.6}\text{La}_{0.2}\text{Ni}_{0.2}\text{O}_{1.7}$	10	0.03	11.2	CeO_2 (50 nm, 0.5476 nm) Ni (traces)
$\text{Ce}_{0.4}\text{La}_{0.4}\text{Ni}_{0.2}\text{O}_{1.6}$	14	0.14	39.8	CeO_2 (50 nm, 0.5598 nm) Ni (traces)
$\text{Ce}_{0.2}\text{La}_{0.6}\text{Ni}_{0.2}\text{O}_{1.5}$	13	0.06	17.5	$\text{La}(\text{OH})_3$ (traces)
$\text{La}_{0.8}\text{Ni}_{0.2}\text{O}_{1.4}$	8	0.02	11.2	$\text{La}(\text{OH})_3$ (traces) Ni (50 nm)
M = Mg				
$\text{Ce}_{0.6}\text{Mg}_{0.2}\text{Ni}_{0.2}\text{O}_{1.6}$	10	0.07	27.7	CeO_2 (25 nm, 0.5415 nm) Ni (25 nm)
$\text{Ce}_{0.4}\text{Mg}_{0.4}\text{Ni}_{0.2}\text{O}_{1.4}$	11	0.05	18.0	CeO_2 (25 nm, 0.5415 nm) Ni (30 nm) MgO (25 nm)
$\text{Ce}_{0.2}\text{Mg}_{0.7}\text{Ni}_{0.1}\text{O}_{1.2}$	19	0.12	26.0	CeO_2 (25 nm, 0.5415 nm) Ni (40 nm) MgO (25 nm)
$\text{Mg}_{0.9}\text{Ni}_{0.1}\text{O}$	23	0.17	29.7	Ni (18 nm) MgO

* In the samples after the reaction, the quartz phase is present in trace amounts. The free volume of the reactor is filled with quartz, and when the reactor is unloaded, it can get into the sample. ** In parentheses are the values of the coherent scattering region and the unit cell parameter.

XRD data show that spent $\text{Ce}_{1-x}\text{Ni}_x\text{O}_y$ samples contain CeO_2 and Ni^0 phases (Figure 24, Table 5), which is similar to the phase composition observed after sample activation (Figure 14, Table 3). However, the phases become less dispersed (50 nm vs. 15–25 nm) as a result of sintering under the reaction conditions, which is typical for supported metal catalysts [31,116]. A similar picture is observed for the $(\text{CeM})_{1-x}\text{Ni}_x\text{O}_y$ samples. A distinctive feature of the La-containing series is the preservation of a CeO_2 -based solid solution after the reaction. Its average crystallite size increases from 20–25 to 50 nm. In contrast to M-free, Al- and La-containing samples, at M = Mg, the sample composition includes three phases (CeO_2 , MgO, and Ni^0) formed at the activation stage (Tables 3 and 5). They grow larger as a result of the reaction. Nevertheless, the ceria phase has an average crystallite size of 25 nm, which is smaller than those for M-free and La-containing samples.

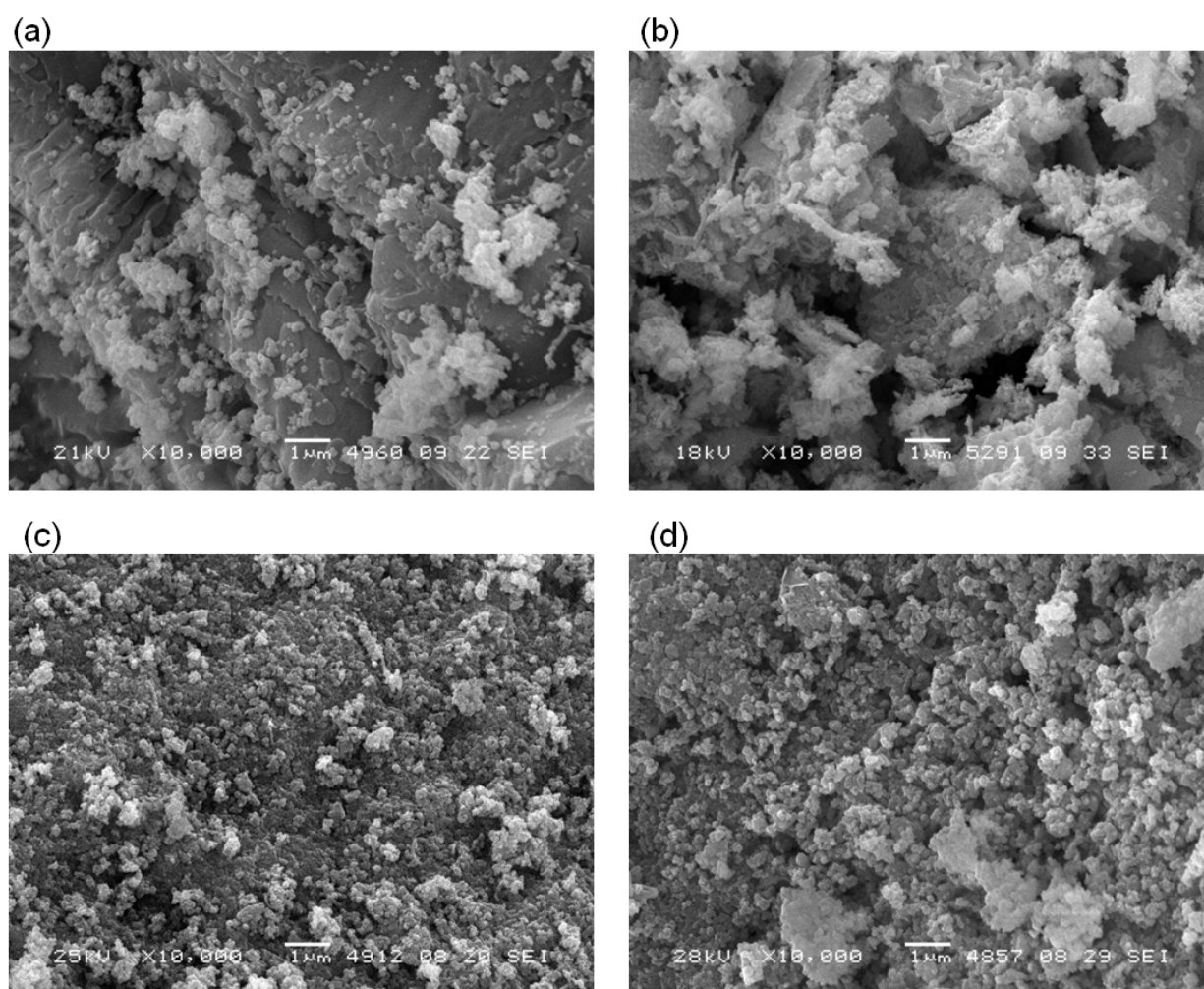


Figure 23. SEM images of spent $(\text{CeM})_{0.8}\text{Ni}_{0.2}\text{O}_y$ samples: without M (a), M = Al (b), La (c) and Mg (d). (b–d)—M/Ce molar ratio is equal to 1. Reaction conditions: 800 °C, 24 h.

According HRTEM study, for all samples, in addition to large, well-crystallized big Ni particles, Ni nanoparticles of 1.5–5 nm in size were observed on the oxide surface. The particles were stabilized due to epitaxy on CeO_2 (a coincidence of the crystallographic directions [111] CeO_2 and [100] Ni is observed) (Figure 25). EDX-mapping of spent samples demonstrates that distribution behavior of M between phases of an individual oxide and CeO_2 -based solid solution is controlled by the type of M. After 24 stability tests, La^{3+} cations remain in the solid solution, Al^{3+} cations only partially remain in the fluorite structure and form Al-enriched crystallites of needle shape, while Mg^{2+} cations prefer to exist outside of the CeO_2 -based solid solution.

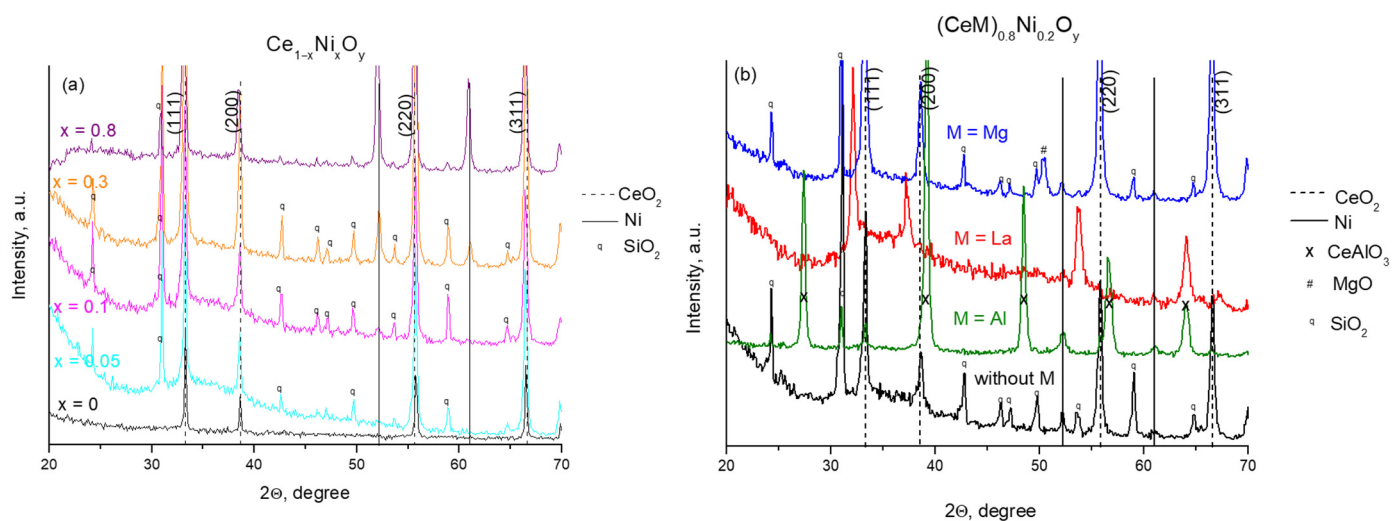


Figure 24. XRD patterns for spent $(\text{CeM})_{1-x}\text{Ni}_x\text{O}_y$ ($M = \text{Al}, \text{La}, \text{Mg}$) samples: effect of Ni molar fraction (a) and M type (b). (b)—M/Ce molar ratio is equal to 1. Reaction conditions: 800 °C, 24 h.

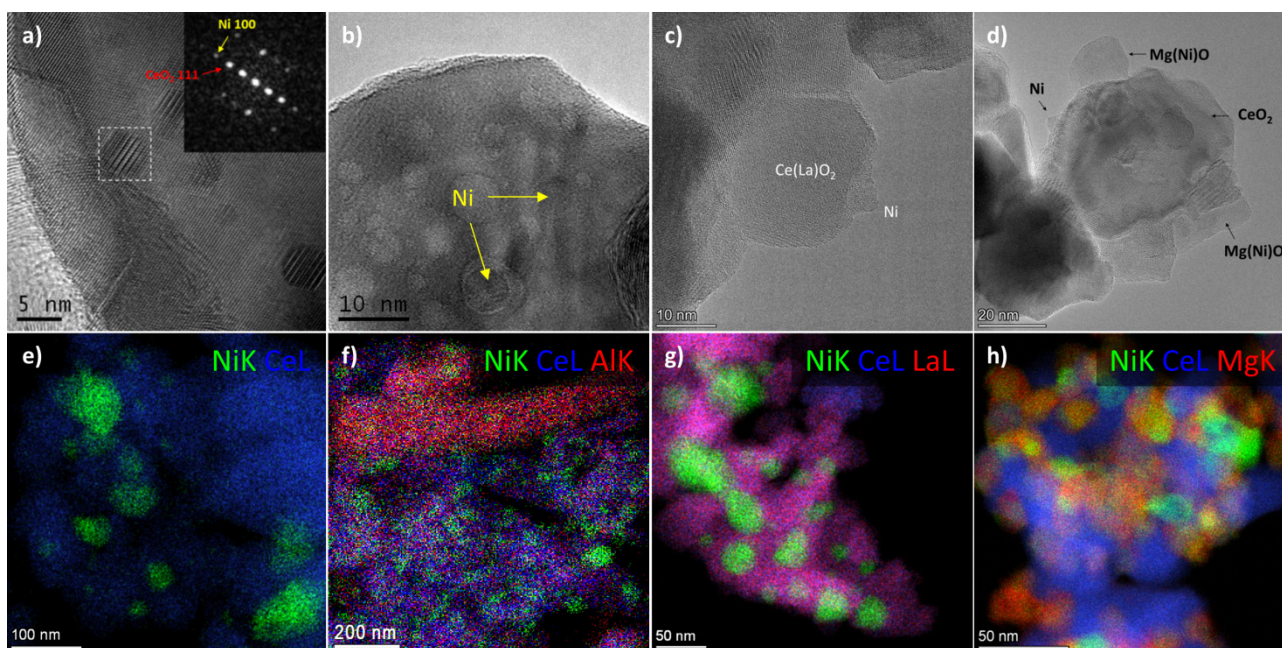


Figure 25. HRTEM pictures (a–d) and EDX mapping (f–h) of spent $\text{Ce}_{0.8}\text{Ni}_{0.2}\text{O}_{1.8}$ (a,e) and $(\text{CeM})_{0.8}\text{Ni}_{0.2}\text{O}_y$ ($M = \text{Al}$ (b,f), La (c,g), Mg (d,h)) samples. M/Ce molar ratio is equal to 1.

Thus, the high activation temperature and subsequent harsh reaction conditions smoothed out the initial textural and structural differences between samples with different values of x . After 24 h during the bi-reforming of methane, spent $\text{Ce}_{1-x}\text{Ni}_x\text{O}_y$ samples were characterized by the same very-low S_{BET} values (3–5 m^2/g) and the phase composition, which is CeO_2 and Ni^0 with a CSR of 50 nm. Nevertheless, with increasing x , first, a higher hydrogen productivity is achieved, and hence a higher hydrogen concentration in the mixture of reaction products, and second, lower deactivation rates are observed. However, the number of carbonaceous deposits is increasing: samples with a lower degree of deactivation ($x = 0.3$) have a higher rate of coke accumulation. It can be assumed that these differences in the activity and stability of the $\text{Ce}_{1-x}\text{Ni}_x\text{O}_y$ samples are more related to the differences in their anti-sintering properties, rather than in their resistance to coke formation. In situ XAS spectroscopy indicates [117] that under reducing conditions

the size and morphology of Ni particles change, as they become flattened and strongly stabilized on the partially reduced CeO₂ surface which promotes their stability under reaction. Taking into account the absence of carbonaceous deposits for spent samples with $x \leq 0.2$, the decrease in activity in the initial period of the reaction before reaching a steady state conversion seems to be mainly associated with phase sintering and a decrease in the number of available active sites. By improving the dispersion of Ni to isolated cations in as-synthesized samples, the Ni particle growth mechanism switches from crystal migration to atomic migration, which leads to higher particle growth rates [31]. Therefore, the sintering process is more pronounced for samples with low values of x , which have higher initial nickel dispersion. Among Ce_{1-x}Ni_xO_y samples, the sample with $x = 0.2$ was chosen as the optimal one due to its ability to provide high and stable conversion of CH₄ and CO₂ to synthesis gas, high H₂ productivity, resistance to the formation of carbon deposits, and a moderate deactivation rate.

The introduction of M into the composition of the samples improves their activity during the bi-reforming of methane. In the case of hydrogen yield, this tendency increases in the series La < Mg < Al. In addition, (CeM)_{1-x}Ni_xO_y samples provide more stable performance with time on stream. In comparison to Ce_{0.8}Ni_{0.2}O_{1.8} samples, (CeM)_{0.8}Ni_{0.2}O_y is characterized by strengthening the Ni-support interaction and a lower rate of thermal sintering. Similar to spent samples without M, (CeM)_{1-x}Ni_xO_y contain coarsely dispersed phases of Ni⁰ and CeO₂. In Al- and Mg-containing systems, the CSR of CeO₂ is lower than those in M-free and La-series samples (25 vs. 50 nm). In contrast to Ce_{0.8}Ni_{0.2}O_{1.8}, (CeM)_{0.8}Ni_{0.2}O_y samples are characterized by coke formation, the rate of which increases in the series Mg < Al < La. This is in good correlation with the structural properties of materials. To be specific, after activation at M = La, the solid solution is preserved, at M = Al, the Al³⁺ cations are only partly retained in the CeO₂ structure, and at M = Mg, the full destruction of solid solution occurs, and CeO₂ and MgO phases co-exist. Given that the M-free sample has better resistance to carbon deposits, this ability is reduced for CeO₂-based solid solutions due to a decrease in the oxygen mobility at a high doping concentration [118].

3. Materials and Methods

3.1. Sample Preparation

The procedure for the synthesis of (CeM)_{1-x}Ni_xO_y (M = Al, La, Mg) solid solutions by the polymerizable complex method was adapted from our previous studies [59,60]. The molar ratio M/Ce varied within 0–4; the mole fraction of Ni in the sample (x) varied from 0.01 to 0.8. The molar fraction of oxygen (y) was calculated based on the principle of electrical neutrality and the assumption that the cations were in the form of Ce⁴⁺, Al³⁺, La³⁺, Mg²⁺, and Ni²⁺. The scheme for the synthesis of catalysts is shown in Figure 1. In these syntheses, cerium nitrate hexahydrate (Ce(NO₃)₃·6H₂O), aluminum nitrate nonahydrate (Al(NO₃)₃·9H₂O), lanthanum nitrate hexahydrate (La(NO₃)₃·6H₂O), magnesium nitrate hexahydrate (Mg(NO₃)₂·6H₂O), nickel nitrate hexahydrate (Ni(NO₃)₂·6H₂O), citric acid monohydrate (CA, C₆H₈O₇·H₂O), ethylene glycol (EG, C₂H₆O₂), and ethylenediamine (ED, C₂H₈N₂) were used as starting materials. The molar ratio of the components was constant and equal to CA:EG:ED:(Ce + M + Ni) = 4:12:4:1.

First, appropriate amounts of metal salts were dissolved in water and mixed with a solution of CA in EG, obtained at 70 °C, with stirring. Then, the resulting solution was stirred at 60 °C for 1 h, and ED was dropwise added to promote the polyesterification reaction. After evaporation at 70 °C for 48 h and the formation of a polymer resin, the sample was thermally treated in a muffle furnace at 500 °C for 4 h in air in order to eliminate the organic matrix. The heat treatment details are given in [60].

For comparison, samples with the same chemical composition were obtained by incipient wetness impregnation of the corresponding Ce_{1-z}M_zO_y (M = Al, La, Mg, $z = 0-1$, $y = 1-2$) supports by an aqueous solution of nickel nitrate with the required concentration.

Supports $Ce_{1-z}M_zO_y$ as reference samples were prepared following the procedure of the PC method used for $(CeM)_{1-x}Ni_xO_y$. These materials were calcined also at 500 °C in air.

3.2. Sample Characterization

The chemical composition of the samples was determined by X-ray fluorescence analysis in an ARL ADVANT'X analyzer (ThermoTechno Scientific, Ecublens, Switzerland) with an Rh anode of the X-ray tube.

Thermogravimetry (TG) and differential thermogravimetry (DTG) with differential thermal analysis (DTA) of polymeric gel and spent catalysts were performed (NETZSCH STA 449C, Selb, Germany) at a heating rate of 10 °C/min up to 900 °C in flowing air.

The N_2 adsorption–desorption isotherms for the samples were measured on an ASAP 2400 automated volumetric instrument (Micromeritics, Norcross, GA, USA) at −196 °C. The specific surface area (S_{BET}) was calculated using the BET method. The total pore volume (V_p) and average pore size (D_p) were calculated using the BJH method applied to the desorption branch of the isotherm.

The scanning electron microscopy (SEM) analysis of the samples was conducted using a JSM-6390LA (JEOL, Tokyo, Japan) electron microscope.

The X-ray diffraction (XRD) analysis of the samples *ex situ* was carried out on an HZG-4C diffractometer (Freiberger Präzisionmechanik, Freiberg, Germany) with CoK_{α} radiation ($\lambda = 1.79021 \text{ \AA}$) at room temperature in the 2θ ranging from 10 to 80° with a step of 0.1 degrees and an accumulation time of 6–15 s. Diffraction peaks were identified using JCPDS powder diffraction databases. Then, according to the Bragg–Wolfe equation, interplanar distances and the parameters of the unit cell (a) were calculated. The accuracy of the determination of the parameters of the unit cell was $\pm 0.003 \text{ \AA}$. The coherent scattering region (CSR) was calculated by the Selyakov–Scherrer method from the broadening of the diffraction peak (111), fixed phases having a cubic structure of the fluorite type; CSR (NiO)—peak (200) phases of NiO; CSR (Ni)—peak (200) phases of Ni^0 .

X-ray phase analysis of the samples *in situ* was conducted on an AXS D8 diffractometer (Bruker, Karlsruhe, Germany) with CuK_{α} radiation ($\lambda = 1.5406 \text{ \AA}$) in the 2θ ranging from 20 to 50° with a step of 0.05 degrees and an accumulation time in each point of 5 s. The heating and cooling rate was 12 °C/s, the exposure time of the diffraction pattern at a certain temperature was at least 30 min before each diffraction pattern was recorded. Parameters of the unit cell were determined using IK 2.1. software (BIC SB RAS, Novosibirsk, Russia) and JCPDS powder diffraction databases.

The Raman spectra of the samples were recorded using an excitation wavelength of 514.5 nm on a Renishaw Invia Raman spectrometer (Renishaw plc., Wotton-under-Edge, Gloucestershire, United Kingdom). The power of the laser radiation incident on the sample did not exceed 2 mW, and the accumulation time was 30 s.

Transmission electron microscopy (TEM) studies were carried out using JEM-2010 (JEOL, Tokyo, Japan), JEM-2200FS (JEOL, Tokyo, Japan) and Themis Z (Thermo Fisher Scientific, Waltham, MA, USA) electron microscopes operated at 200 kV. Images in Scanning-TEM (STEM) mode were acquired using high-angle annular dark field (HAADF) detectors. The local elemental analysis of the samples was studied by energy-dispersive X-ray (EDX) spectroscopy using a JEOL JED-2300 (JEM-2200FS) and Thermo Fisher Scientific Super-X (THEMIS Z) EDX detectors. The samples for the TEM studies were dispersed ultrasonically and deposited on copper grids covered with a holey carbon film.

The temperature-programmed hydrogen reduction (H_2 -TPR) was performed on a setup equipped with a flow reactor and a thermal conductivity detector [119]. To eliminate exothermic effects, a 100 mg sample with a size of 250–500 μm was mixed with 100 mg of quartz of the same size. The sample was then pre-treated at 450 °C for 1 h in a stream of air. The reduction was carried out at a heating rate of 10 °C/min from 25 to 900 °C in a flow of 10% H_2 /90% Ar, 30 cm^3/min .

3.3. Catalytic Activity Testing

The bi-reforming of CH₄ over prepared catalysts was studied in a fixed-bed flow quartz reactor with an inner diameter of 10 mm, at 1 atm, a gas flow rate of 200 ml_N/min, and a molar ratio between reagents of CH₄:CO₂:H₂O:He = 1:0.8:0.4:2.8. The molar ratio used was somewhat different from the stoichiometric CH₄:CO₂:H₂O molar ratio of 1:0.5:0.5. A higher CO₂/H₂O ratio (0.8 vs. 0.5) was applied in order to increase carbon dioxide utilization, while a higher O/C ratio (1.1 vs. 1) was used to reduce the rate of coking. Water was supplied by a piston pump at the required rate to the evaporator, where water vapor was mixed with other components (CH₄, CO₂, He) and quantitatively introduced into the fixed-bed reactor.

For catalytic activity testing, a 500 mg sample with a grain size of 250–500 μm was used. Initially, the activation of catalyst precursors was performed in situ by thermal treatment at 800 °C for 1 h in a 30% H₂/70% He flow.

The screening tests were performed in the stepwise temperature rise mode 650 → 850 °C. The heating rate was 10 degrees per minute; the holding time at each temperature was 40 min.

The stability tests were performed for 24 h at 800 °C.

The analysis of reaction mixtures was performed using the online automatic gas chromatography system Kristall 2000 m (Yoshkar-Ola, Russia) with a flame ionization detector and thermal conductivity detector.

The catalyst performance was characterized by CH₄ conversion (X_{CH_4}), CO₂ conversion (X_{CO_2}), yield of H₂ (Y_{H_2}), and yield of CO (Y_{CO}), which were calculated using the following formulas:

$$\text{CH}_4 \text{ conversion : } X_{CH_4} = 100 \times \left(F_{CH_4}^{\text{in}} - F_{CH_4}^{\text{out}} \right) / F_{CH_4}^{\text{in}}$$

$$\text{CO}_2 \text{ conversion : } X_{CO_2} = 100 \times \left(F_{CO_2}^{\text{in}} - F_{CO_2}^{\text{out}} \right) / F_{CO_2}^{\text{in}}$$

$$\text{H}_2 \text{ yield : } Y_{H_2} = 100 \times F_{H_2}^{\text{out}} / \left(2F_{CH_4}^{\text{in}} + F_{H_2O}^{\text{in}} \right)$$

$$\text{CO yield : } Y_{CO} = 100 \times F_{CO}^{\text{out}} / \left(F_{CH_4}^{\text{in}} + F_{CO_2}^{\text{in}} \right)$$

where F_i is the molar flow rate of reagent (i) at the inlet (in) and outlet (out) of the reactor.

The thermodynamic equilibrium analysis was conducted using the software package IVTANTHERMO based on the minimization of the Gibbs free energy method [120,121].

4. Conclusions

Thus, (CeM)_{1-x}Ni_xO_y (M = Al, La, Mg) materials served as precursors of Ni catalysts during the bi-reforming of methane. Their genesis features as well as textural, structural, and redox characteristics and functional properties were regulated by variation in the type and content of M. In comparison to the M-free sample, for (CeM)_{1-x}Ni_xO_y with an optimal M/Ce ratio, the size of crystallites decreases, the defectiveness and the thermal stability of the material increases, and the temperature of formation of the active Ni⁰ phase rises (ΔT = 100–200 °C), while the temperature of its re-oxidation decreases (ΔT = 70 °C). This all results in the improvement of the strength of the metal–support interaction and provides a more stable and higher yield of hydrogen.

In the case of M = Al, the as-synthesized samples have a homogenous phase composition of a solid fluorite-like solution with mesoporous texture and spongy morphology. Among studied M, the Al-series is characterized by the highest burnout temperature of the organic matrix during synthesis by the PC method, a higher specific surface area, and the smallest solid solution crystallite size (CSR 2.8–4.5 nm). For higher specific surface area (80–100 m²/g) the Al/Ce molar ratio should be equal to ≤1. In (CeAl)_{1-x}Ni_xO_y samples, the cations of Ni²⁺ are stabilized in the structure of a solid solution and their exsolution under a reducing atmosphere leads to the formation of the Ni⁰ phase at 600 °C. A feature of the Al-series is that, under activation and reaction conditions, a complete transformation

of the oxide matrix occurs: CeO_2 -based solid solution $\rightarrow \text{Ni}^0$ + cerium aluminate of perovskite structure ($\text{Al}/\text{Ce} = 1$). This is accompanied by a significant decrease in the specific surface area and pore volume. $(\text{CeAl})_{1-x}\text{Ni}_x\text{O}_y$ samples provide the highest H_2 yield for the bi-reforming of methane and moderate stability against coking.

In the case of $M = \text{La}$ and synthesis by the PC method, the formation of a solid fluorite-like solution (CSR 4.0–6.0 nm) with the highest concentration of oxygen vacancies is observed, and only an insignificant fraction of nickel is stabilized as NiO nanoparticles (3–5 nm) on the sample surface. Among studied M , for samples of the La-series, the burnout of the organic matrix occurs at the lowest temperature. They are characterized by a rapid decrease in the specific surface area and an increase of the defectiveness of the structure with increasing La/Ce molar ratio. A feature of the La-series is that the exsolution of Ni from solid solution is highly hindered, and the Ni^0 phase appears only at a reduction temperature of 650 °C, while the Ce-La-O-solid solution remains. $(\text{CeLa})_{1-x}\text{Ni}_x\text{O}_y$ samples provide the lowest H_2 yield for the bi-reforming of methane and poor stability against coking.

In the case of $M = \text{Mg}$, a two-phase system is already observed for the freshly synthesized sample, which may be due to the low stability of the Mg–citrate complex and partial segregation of the MgO phase at the earliest stage of the complex oxide formation. Therefore, in addition to a solid fluorite-like solution, the formation of a NiO-MgO solid solution (CSR 3.6–8.5 nm) is observed. Due to this, samples have the lowest reducibility. After activation, a three-phase system is formed, including Ni^0 , MgO, and a CeO_2 -based fluorite-like phase. $(\text{CeMg})_{1-x}\text{Ni}_x\text{O}_y$ samples provide high H_2 yield during the bi-reforming of methane and the highest stability against coking.

Taking into account three factors (activity, stability, and the coke accumulation rate), the efficiency of methane bi-reforming catalysts increases in the following order: M -free < La < Al < Mg. The composition $\text{Ce}_{0.6}\text{Mg}_{0.4}\text{Ni}_{0.2}\text{O}_{1.6}$ is considered the best. During the bi-reforming of methane over $\text{Ce}_{0.6}\text{Mg}_{0.4}\text{Ni}_{0.2}\text{O}_{1.6}$, a stable H_2 yield of 90% is achieved at a high level of CO_2 and CH_4 conversions (>85%).

Author Contributions: Conceptualization, M.K. and E.M.; methodology, E.M.; synthesis, E.M.; formal analysis, O.S. (Olga Sukhova); investigation, I.I., S.Y., V.U., O.S. (Olga Stonkus), E.G., A.N. and P.B.; data curation, M.K.; writing—original draft preparation, E.M.; writing—review and editing, E.M. and M.K.; supervision, Z.I. All authors have read and agreed to the published version of the manuscript.

Funding: This work was supported by the Ministry of Science and Higher Education of the Russian Federation within the governmental order for the Boreskov Institute of Catalysis (project AAAA-A21-121011490008-3).

Data Availability Statement: Data is contained within the article.

Acknowledgments: The TEM and SEM studies were carried out using facilities of the shared research center “National center of investigation of catalysts” at the Boreskov Institute of Catalysis. The authors also acknowledge the resource center “VTAN” (Novosibirsk State University) for granting access to TEM equipment. The authors are grateful to A.A. Pochtar and A.A. Leonova for their assistance with catalyst characterization.

Conflicts of Interest: The authors declare no conflict of interest.

References

1. Birol, F. The Future of Hydrogen: Seizing Today’s Opportunities. Available online: https://www.hydrogenexpo.com/media/9370/the_future_of_hydrogen_iaea.pdf (accessed on 1 November 2022).
2. International Energy Agency. Cross-Cutting: Hydrogen. 2020. Available online: <https://www.ceguide.org/wp-content/uploads/2020/08/07-IEA-Cross-cutting.pdf> (accessed on 1 November 2022).
3. Lebrouhi, B.E.; Djoupo, J.J.; Lamrani, B.; Benabdelaziz, K.; Kousksou, T. Global hydrogen development—A technological and geopolitical overview. *Int. J. Hydrogen Energy* **2022**, *47*, 7016–7048. [CrossRef]
4. Pal, D.B.; Singh, A.; Bhatnagar, A. A review on biomass based hydrogen production technologies. *Int. J. Hydrogen Energy* **2022**, *47*, 1461–1480. [CrossRef]
5. Faye, O.; Szpunar, J.; Eduok, U. A critical review on the current technologies for the generation, storage, and transportation of hydrogen. *Int. J. Hydrogen Energy* **2022**, *47*, 13771–13802. [CrossRef]

6. Yu, M.; Wang, K.; Vredenburg, H. Insights into low-carbon hydrogen production methods: Green, blue and aqua hydrogen. *Int. J. Hydrogen Energy* **2021**, *46*, 21261–21273. [CrossRef]
7. Matus, E.; Sukhova, O.; Ismagilov, I.; Kerzhentsev, M.; Stonkus, O.; Ismagilov, Z. Hydrogen production through autothermal reforming of ethanol: Enhancement of Ni catalyst performance via promotion. *Energies* **2021**, *14*, 5176. [CrossRef]
8. Matus, E.V.; Ismagilov, I.Z.; Mikhaylova, E.S.; Ismagilov, Z.R. Hydrogen Production from Coal Industry Methane. *Eurasian Chem.-Technol. J.* **2022**, *24*, 69–91. [CrossRef]
9. Howarth, R.W.; Jacobson, M.Z. How green is blue hydrogen? *Energy Sci. Eng.* **2021**, *9*, 1676–1687. [CrossRef]
10. IEA. Net Zero by 2050: A Roadmap for the Global Energy Sector. International Energy Agency, 2021. Available online: <https://www.iea.org/reports/net-zero-by-2050> (accessed on 1 November 2022).
11. Quarton, C.J.; Samsatli, S. The value of hydrogen and carbon capture, storage and utilisation in decarbonising energy: Insights from integrated value chain optimisation. *Appl. Energy* **2020**, *257*, 113936. [CrossRef]
12. Deng, J.; Chu, W.; Wang, B.; Yang, W.; Zhao, X.S. Mesoporous Ni/Ce_{1-x}Ni_xO_{2-y} heterostructure as an efficient catalyst for converting greenhouse gas to H₂ and syngas. *Catal. Sci. Technol.* **2016**, *6*, 851–862. [CrossRef]
13. Batebi, D.; Abedini, R.; Mosayebi, A. Combined steam and CO₂ reforming of methane (CSCRM) over Ni–Pd/Al₂O₃ catalyst for syngas formation. *Int. J. Hydrogen Energy* **2020**, *45*, 14293–14310. [CrossRef]
14. Cunha, A.F.; Morales-Torres, S.; Pastrana-Martínez, L.M.; Maldonado-Hódar, F.J.; Caetano, N.S. Syngas production by bi-reforming of methane on a bimetallic Ni-ZnO doped zeolite 13X. *Fuel* **2022**, *311*, 122592. [CrossRef]
15. Peng, J.B.; Geng, H.Q.; Wu, X.F. The Chemistry of CO: Carbonylation. *Chem* **2019**, *5*, 526–552. [CrossRef]
16. Qi, J.; Christopher, P. Atomically dispersed rh active sites on oxide supports with controlled acidity for gas-phase halide-free methanol carbonylation to acetic acid. *Ind. Eng. Chem. Res.* **2019**, *58*, 12632–12641. [CrossRef]
17. Qi, J.; Finzel, J.; Robatjazi, H.; Xu, M.; Hoffman, A.S.; Bare, S.R.; Pan, X.; Christopher, P. Selective Methanol Carbonylation to Acetic Acid on Heterogeneous Atomically Dispersed ReO₄/SiO₂ Catalysts. *J. Am. Chem. Soc.* **2020**, *142*, 14178–14189. [CrossRef]
18. Dall’Anese, A.; Fiorindo, M.; Olivieri, D.; Carfagna, C.; Balducci, G.; Alessio, E.; Durand, J.; Milani, B. Pd-Catalyzed CO/Vinyl Arene Copolymerization: When the Stereochemistry is Controlled by the Comonomer. *Macromolecules* **2020**, *53*, 7783–7794. [CrossRef]
19. Stadler, B.M.; Wulf, C.; Werner, T.; Tin, S.; De Vries, J.G. Catalytic Approaches to Monomers for Polymers Based on Renewables. *ACS Catal.* **2019**, *9*, 8012–8067. [CrossRef]
20. Jang, W.J.; Jeong, D.W.; Shim, J.O.; Kim, H.M.; Roh, H.S.; Son, I.H.; Lee, S.J. Combined steam and carbon dioxide reforming of methane and side reactions: Thermodynamic equilibrium analysis and experimental application. *Appl. Energy* **2016**, *173*, 80–91. [CrossRef]
21. Matus, E.V.; Sukhova, O.B.; Ismagilov, I.Z.; Kerzhentsev, M.A.; Li, L.; Ismagilov, Z.R. Bi-reforming of methane: Thermodynamic equilibrium analysis and selection of preferable reaction conditions. *J. Phys. Conf. Ser.* **2021**, *1749*, 012023. [CrossRef]
22. Chen, L.; Qi, Z.; Zhang, S.; Su, J.; Somorjai, G.A. Catalytic hydrogen production from methane: A review on recent progress and prospect. *Catalysts* **2020**, *10*, 858. [CrossRef]
23. Ismagilov, Z.R.; Matus, E.V.; Ismagilov, I.Z.; Sukhova, O.B.; Yashnik, S.A.; Ushakov, V.A.; Kerzhentsev, M.A. Hydrogen production through hydrocarbon fuel reforming processes over Ni based catalysts. *Catal. Today* **2019**, *323*, 166–182. [CrossRef]
24. Abdullah, B.; Abd Ghani, N.A.; Vo, D.V.N. Recent advances in dry reforming of methane over Ni-based catalysts. *J. Clean. Prod.* **2017**, *162*, 170–185. [CrossRef]
25. Pham, X.H.; Ashik, U.P.M.; Hayashi, J.I.; Alonso, A.P.; Pla, D.; Gómez, M.; Minh, D.P. Review on the catalytic tri-reforming of methane—Part II: Catalyst development. *Appl. Catal. A Gen.* **2021**, *623*, 118286. [CrossRef]
26. Matus, E.V.; Ev, S.D.V.; Ismagilov, I.Z.; Ushakov, V.A.; Kerzhentsev, O.A.; Ismagilov, Z.R. Development of Supported Ni Catalysts for Autothermal Reforming of Methane. *Chem. Sustain. Dev.* **2020**, *28*, 403–411. [CrossRef]
27. Mierczynski, P.; Mosinska, M.; Stepinska, N.; Chalupka, K.; Nowosielska, M.; Maniukiewicz, W.; Rogowski, J.; Goswami, N.; Vasilev, K.; Szyrkowska, M.I. Effect of the support composition on catalytic and physicochemical properties of Ni catalysts in oxy-steam reforming of methane. *Catal. Today* **2021**, *364*, 46–60. [CrossRef]
28. Zagaynov, I.V. Active Components of Catalysts of Methane Conversion to Synthesis Gas: Brief Perspectives. *Energy Fuels* **2021**, *35*, 9124–9136. [CrossRef]
29. Matus, E.V.; Ismagilov, I.Z.; Yashnik, S.A.; Ushakov, V.A.; Prosvirin, I.P.; Kerzhentsev, M.A.; Ismagilov, Z.R. Hydrogen production through autothermal reforming of CH₄: Efficiency and action mode of noble (M = Pt, Pd) and non-noble (M = Re, Mo, Sn) metal additives in the composition of Ni-M/Ce_{0.5}Zr_{0.5}O₂/Al₂O₃ catalysts. *Int. J. Hydrogen Energy* **2020**, *45*, 33352–33369. [CrossRef]
30. Matus, E.V.; Shlyakhtina, A.S.; Sukhova, O.B.; Ismagilov, I.Z.; Ushakov, V.A.; Yashnik, S.A.; Nikitin, A.P.; Bharali, P.; Kerzhentsev, M.A.; Ismagilov, Z.R. Effect of Preparation Methods on the Physicochemical and Functional Properties of Ni/CeO₂ Catalysts. *Kinet. Catal.* **2019**, *60*, 221–230. [CrossRef]
31. Lyu, Y.; Jocz, J.; Xu, R.; Stavitski, E.; Sievers, C. Nickel Speciation and Methane Dry Reforming Performance of Ni/Ce_xZr_{1-x}O₂ Prepared by Different Synthesis Methods. *ACS Catal.* **2020**, *10*, 11235–11252. [CrossRef]
32. Khani, Y.; Bahadoran, F.; Shariatina, Z.; Varmazyari, M.; Safari, N. Synthesis of highly efficient and stable Ni/Ce_xZr_{1-x}Gd_xO₄ and Ni/X-Al₂O₃ (x = Ce, Zr, Gd, Ce-Zr-Gd) nanocatalysts applied in methane reforming reactions. *Ceram. Int.* **2020**, *46*, 25122–25135. [CrossRef]

33. Matus, E.V.; Nefedova, D.V.; Kuznetsov, V.V.; Ushakov, V.A.; Stonkus, O.A.; Ismagilov, I.Z.; Kerzhentsev, M.A.; Ismagilov, Z.R. Effect of the support composition on the physicochemical properties of Ni/Ce_{1-x}La_xO_y catalysts and their activity in an autothermal methane reforming reaction. *Kinet. Catal.* **2017**, *58*, 610–621. [\[CrossRef\]](#)
34. Cheephat, C.; Daorattanachai, P.; Devahastin, S.; Laosiripojana, N. Partial oxidation of methane over monometallic and bimetallic Ni-, Rh-, Re-based catalysts: Effects of Re addition, co-fed reactants and catalyst support. *Appl. Catal. A Gen.* **2018**, *563*, 1–8. [\[CrossRef\]](#)
35. Ismagilov, I.Z.; Vosmerikov, A.V.; Korobitsyna, L.L.; Matus, E.V.; Kerzhentsev, M.A.; Stepanov, A.A.; Mihaylova, E.S.; Ismagilov, Z.R. Promoters for improvement of the catalyst performance in methane valorization processes. *Eurasian Chem.-Technol. J.* **2021**, *23*, 147–168. [\[CrossRef\]](#)
36. da Fonseca, R.O.; Pongeggi, A.R.; Rabelo-Neto, R.C.; Simões, R.C.C.; Mattos, L.V.; Noronha, F.B. Controlling carbon formation over Ni/CeO₂ catalyst for dry reforming of CH₄ by tuning Ni crystallite size and oxygen vacancies of the support. *J. CO₂ Util.* **2022**, *57*, 101880. [\[CrossRef\]](#)
37. Juan-Juan, J.; Román-Martínez, M.C.; Illán-Gómez, M.J. Nickel catalyst activation in the carbon dioxide reforming of methane. Effect of pretreatments. *Appl. Catal. A Gen.* **2009**, *355*, 27–32. [\[CrossRef\]](#)
38. Pino, L.; Italiano, C.; Vita, A.; Laganà, M.; Recupero, V. Ce_{0.70}La_{0.20}Ni_{0.10}O_{2-Δ} catalyst for methane dry reforming: Influence of reduction temperature on the catalytic activity and stability. *Appl. Catal. B Environ.* **2017**, *218*, 779–792. [\[CrossRef\]](#)
39. Sokolov, S.; Kondratenko, E.V.; Pohl, M.M.; Rodemerck, U. Effect of calcination conditions on time on-stream performance of Ni/La₂O₃-ZrO₂ in low-temperature dry reforming of methane. *Int. J. Hydrogen Energy* **2013**, *38*, 16121–16132. [\[CrossRef\]](#)
40. Feng, X.; Feng, J.; Li, W. Insight into MgO promoter with low concentration for the carbon-deposition resistance of Ni-based catalysts in the CO₂ reforming of CH₄. *Cuihua Xuebao/Chin. J. Catal.* **2018**, *39*, 88–98. [\[CrossRef\]](#)
41. Al-Fatesh, A.S.; Naeem, M.A.; Fakeeha, A.H.; Abasaed, A.E. Role of La₂O₃ as Promoter and Support in Ni/γ-Al₂O₃ Catalysts for Dry Reforming of Methane. *Chin. J. Chem. Eng.* **2014**, *22*, 28–37. [\[CrossRef\]](#)
42. Damaskinos, C.M.; Zavašnik, J.; Djinović, P.; Efstathiou, A.M. Dry reforming of methane over Ni/Ce_{0.8}Ti_{0.2}O_{2-δ}: The effect of Ni particle size on the carbon pathways studied by transient and isotopic techniques. *Appl. Catal. B Environ.* **2021**, *296*, 120321. [\[CrossRef\]](#)
43. Liu, Z.; Duchoň, T.; Wang, H.; Grinter, D.C.; Waluyo, I.; Zhou, J.; Liu, Q.; Jeong, B.; Crumlin, E.J.; Matolín, V.; et al. Ambient pressure XPS and IRRAS investigation of ethanol steam reforming on Ni-CeO₂(111) catalysts: An: In situ study of C-C and O-H bond scission. *Phys. Chem. Chem. Phys.* **2016**, *18*, 16621–16628. [\[CrossRef\]](#) [\[PubMed\]](#)
44. Salcedo, A.; Lustemberg, P.G.; Rui, N.; Palomino, R.M.; Liu, Z.; Nemsak, S.; Senanayake, S.D.; Rodriguez, J.A.; Ganduglia-Pirovano, M.V.; Irigoyen, B. Reaction Pathway for Coke-free methane steam reforming on a Ni/CeO₂ Catalyst: Active Sites and the Role of Metal-Support Interactions. *ACS Catal.* **2021**, *11*, 8327–8337. [\[CrossRef\]](#)
45. Lustemberg, P.G.; Mao, Z.; Salcedo, A.; Irigoyen, B.; Ganduglia-Pirovano, M.V.; Campbell, C.T. Nature of the Active Sites on Ni/CeO₂ Catalysts for Methane Conversions. *ACS Catal.* **2021**, *11*, 10604–10613. [\[CrossRef\]](#) [\[PubMed\]](#)
46. Singha, R.K.; Tsuji, Y.; Mahyuddin, M.H.; Yoshizawa, K. Methane Activation at the Metal-Support Interface of Ni₄-CeO₂(111) Catalyst: A Theoretical Study. *J. Phys. Chem. C* **2019**, *123*, 9788–9798. [\[CrossRef\]](#)
47. Lian, Z.; Olanrele, S.O.; Si, C.; Yang, M.; Li, B. Critical Role of Interfacial Sites between Nickel and CeO₂ Support in Dry Reforming of Methane: Revisit of Reaction Mechanism and Origin of Stability. *J. Phys. Chem. C* **2020**, *124*, 5118–5124. [\[CrossRef\]](#)
48. Carrasco, J.; López-Durán, D.; Liu, Z.; Duchoň, T.; Evans, J.; Senanayake, S.D.; Crumlin, E.J.; Matolín, V.; Rodríguez, J.A.; Ganduglia-Pirovano, M.V. In situ and theoretical studies for the dissociation of water on an active Ni/CeO₂ Catalyst: Importance of strong metal-support interactions for the cleavage of O-H bonds. *Angew. Chem. Int. Ed.* **2015**, *54*, 3917–3921. [\[CrossRef\]](#)
49. Gao, X.; Li, J.; Zheng, M.; Cai, S.; Zhang, J.; Askari, S.; Dewangan, N.; Ashok, J.; Kawi, S. Recent progress in anti-coking Ni catalysts for thermo-catalytic conversion of greenhouse gases. *Process. Saf. Environ. Prot.* **2021**, *156*, 598–616. [\[CrossRef\]](#)
50. Cop, P.; Maile, R.; Sun, Y.; Khalid, O.; Djerdj, I.; Esch, P.; Heiles, S.; Over, H.; Smarsly, B.M. Impact of Aliovalent/Isovalent Ions (Gd, Zr, Pr, and Tb) on the Catalytic Stability of Mesoporous Ceria in the HCl Oxidation Reaction. *ACS Appl. Nano Mater.* **2020**, *3*, 7406–7419. [\[CrossRef\]](#)
51. Kerzhentsev, M.A.; Matus, E.V.; Ismagilov, I.Z.; Ushakov, V.A.; Stonkus, O.A.; Larina, T.V.; Kozlova, G.S.; Bharali, P.; Ismagilov, Z.R. Structural and morphological properties of Ce_{1-x}M_xO_y (M = Gd, La, Mg) supports for the catalysts of autothermal ethanol conversion. *J. Struct. Chem.* **2017**, *58*, 126–134. [\[CrossRef\]](#)
52. Yu, Q.; Wu, X.; Tang, C.; Qi, L.; Liu, B.; Gao, F.; Sun, K.; Dong, L.; Chen, Y. Textural, structural, and morphological characterizations and catalytic activity of nanosized CeO₂-MO_x (M = Mg²⁺, Al³⁺, Si⁴⁺) mixed oxides for CO oxidation. *J. Colloid Interface Sci.* **2011**, *354*, 341–352. [\[CrossRef\]](#)
53. Matus, E.V.; Okhlopkova, L.B.; Sukhova, O.B.; Ismagilov, I.Z.; Kerzhentsev, M.A.; Ismagilov, Z.R. Effects of preparation mode and doping on the genesis and properties of Ni/Ce_{1-x}M_xO_y nanocrystallites (M = Gd, La, Mg) for catalytic applications. *J. Nanopart. Res.* **2019**, *21*, 11. [\[CrossRef\]](#)
54. Kumar, P.; Matoh, L.; Kaur, R.; Štangar, U.L. Synergic effect of manganese oxide on ceria based catalyst for direct conversion of CO₂ to green fuel additive: Catalyst activity and thermodynamics study. *Fuel* **2021**, *285*, 119083. [\[CrossRef\]](#)
55. Pakharukova, V.P.; Potemkin, D.I.; Stonkus, O.A.; Kharchenko, N.A.; Saraev, A.A.; Gorlova, A.M. Investigation of the Structure and Interface Features of Ni/Ce_{1-x}Zr_xO₂ Catalysts for CO and CO₂ Methanation. *J. Phys. Chem. C* **2021**, *125*, 20538–20550. [\[CrossRef\]](#)
56. Wang, F.; Wei, M.; Evans, D.G.; Duan, X. CeO₂-based heterogeneous catalysts toward catalytic conversion of CO₂. *J. Mater. Chem. A* **2016**, *4*, 5773–5783. [\[CrossRef\]](#)

57. Li, X.; Zhao, Z.J.; Zeng, L.; Zhao, J.; Tian, H.; Chen, S.; Li, K.; Sang, S.; Gong, J. On the role of Ce in CO₂ adsorption and activation over lanthanum species. *Chem. Sci.* **2018**, *9*, 3426–3437. [CrossRef]
58. Zhang, F.; Liu, Z.; Chen, X.; Rui, N.; Betancourt, L.E.; Lin, L.; Xu, W.; Sun, C.J.; Abeykoon, A.M.; Rodriguez, J.A.; et al. Effects of Zr Doping into Ceria for the Dry Reforming of Methane over Ni/CeZrO₂ Catalysts: In Situ Studies with XRD, XAFS, and AP-XPS. *ACS Catal.* **2020**, *10*, 3274–3284. [CrossRef]
59. Matus, E.V.; Ismagilov, I.Z.; Ushakov, V.A.; Nikitin, A.P.; Stonkus, O.A.; Gerasimov, E.Y.; Kerzhentsev, M.A.; Bharali, P.; Ismagilov, Z.R. Genesis and structural properties of (Ce_{1-x}M_x)_{0.8}Ni_{0.2}O_y (M = La, Mg) oxides. *J. Struct. Chem.* **2020**, *61*, 1080–1089. [CrossRef]
60. Matus, E.V.; Nefedova, D.V.; Sukhova, O.B.; Ismagilov, I.Z.; Ushakov, V.A.; Yashnik, S.A.; Nikitin, A.P.; Kerzhentsev, M.A.; Ismagilov, Z.R. Formation and Properties of Ni–Ce–La–O Catalysts of Reforming. *Kinet. Catal.* **2019**, *60*, 496–507. [CrossRef]
61. Tao, K.; Zhou, S.; Zhang, Q.; Kong, C.; Ma, Q.; Tsubaki, N.; Chen, L. Sol-gel auto-combustion synthesis of Ni-Ce_xZr_{1-x}O₂ catalysts for carbon dioxide reforming of methane. *RSC Adv.* **2013**, *3*, 22285–22294. [CrossRef]
62. Liu, F.; Zhao, L.; Wang, H.; Bai, X.; Liu, Y. Study on the preparation of Ni-La-Ce oxide catalyst for steam reforming of ethanol. *Int. J. Hydrogen Energy* **2014**, *39*, 10454–10466. [CrossRef]
63. Ponchel, A.; D’huysser, A.; Lamonier, C.; Jalowiecki-duhamel, L. CeNiO and CeAlNiO solids studied by electron microscopy. *Phys. Chem. Chem. Phys.* **2000**, *2*, 303–312. [CrossRef]
64. Sun, X.; Chen, H.; Yin, Y.; Curnan, M.T.; Han, J.W.; Chen, Y.; Ma, Z. Progress of Exsolved Metal Nanoparticles on Oxides as High Performance (Electro)Catalysts for the Conversion of Small Molecules. *Small* **2021**, *17*, 2005383. [CrossRef] [PubMed]
65. Kwon, O.; Joo, S.; Choi, S.; Sengodan, S.; Kim, G. Review on exsolution and its driving forces in perovskites. *J. Phys. Energy* **2020**, *2*, 032001. [CrossRef]
66. Kousi, K.; Neagu, D.; Metcalfe, I.S. Combining Exsolution and Infiltration for Redox, Low Temperature CH₄ Conversion to Syngas. *Catalysts* **2020**, *10*, 468. [CrossRef]
67. Rodriguez, J.A.; Grinter, D.C.; Liu, Z.; Palomino, R.M.; Senanayake, S.D. Ceria-based model catalysts: Fundamental studies on the importance of the metal-ceria interface in CO oxidation, the water-gas shift, CO₂ hydrogenation, and methane and alcohol reforming. *Chem. Soc. Rev.* **2017**, *46*, 1824–1841. [CrossRef] [PubMed]
68. Mueller, V.H.; Duduković, M.P.; Lo, C.S. The role of metal-support interaction on catalytic methane activation. *Appl. Catal. A Gen.* **2014**, *488*, 138–147. [CrossRef]
69. Romero-Núñez, A.; Díaz, G. High oxygen storage capacity and enhanced catalytic performance of NiO/Ni_xCe_{1-x}O_{2-δ} nanorods: Synergy between Ni-doping and 1D morphology. *RSC Adv.* **2015**, *5*, 54571–54579. [CrossRef]
70. Barrio, L.; Kubacka, A.; Zhou, G.; Estrella, M.; Martinez-Arias, A.; Hanson, J.C.; Fernandez-Garcia, M.; Rodriguez, J.A. Unusual physical and chemical properties of ni in Ce_{1-x}Ni_xO_{2-y} oxides: Structural characterization and catalytic activity for the water gas shift reaction. *J. Phys. Chem. C* **2010**, *114*, 12689–12697. [CrossRef]
71. Kerzhentsev, M.A.; Matus, E.V.; Ismagilov, I.Z.; Sukhova, O.B.; Bharali, P.; Ismagilov, Z.R. Control of Ni/Ce_{1-x}M_xO_y catalyst properties via the selection of dopant M = Gd, La, Mg. Part 1. physicochemical characteristics. *Eurasian Chem. J.* **2018**, *20*, 283–291. [CrossRef]
72. Gondim, M.S.; Silva, E.C.; dos Santos, A.L.; de Assis, M.; Mercury, J.M.; Leite, E.R.; Nogueira, I.C. Synthesis of ZnWO₄ by the polymerizable complex method: Evidence of amorphous phase coexistence during the phase formation process. *Ceram. Int.* **2021**, *47*, 19073–19078. [CrossRef]
73. Stability Constants of Complex Compounds. Available online: <https://www.freechemistry.ru/cen3.htm> (accessed on 26 April 2022).
74. Li, Y.; Huo, Y.; Li, C.; Xing, S.; Liu, L.; Zou, G. Thermal analysis of Cu-organic composite nanoparticles and fabrication of highly conductive copper films. *J. Alloys Compd.* **2015**, *649*, 1156–1163. [CrossRef]
75. Sing, K.S.W.; Williams, R.T. Physisorption Hysteresis Loops and the Characterization of Nanoporous Materials. *Adsorpt. Sci. Technol.* **2004**, *22*, 773–782. [CrossRef]
76. El Hannach, M.; Soboleva, T.; Malek, K.; Franco, A.A.; Prat, M.; Pauchet, J.; Holdcroft, S. Characterization of pore network structure in catalyst layers of polymer electrolyte fuel cells. *J. Power Sources* **2014**, *247*, 322–326. [CrossRef]
77. Zhao, P.; Qin, F.; Huang, Z.; Sun, C.; Shen, W.; Xu, H. Morphology-dependent oxygen vacancies and synergistic effects of Ni/CeO₂ catalysts for N₂O decomposition. *Catal. Sci. Technol.* **2018**, *8*, 276–288. [CrossRef]
78. Chen, P.-L.; Chen, I.-W. Grain Growth in CeO₂: Dopant Effects, Defect Mechanism, and Solute Drag. *J. Am. Ceram. Soc.* **1996**, *79*, 1793–1800. [CrossRef]
79. Khandale, K.N.A.; Bhoga, S. Synthesis and characterization of nanocrystalline Gd doped CeO₂. *Asian J. Chem.* **2009**, *21*, 13–16.
80. Wu, L.; Wiesmann, H.J.; Moodenbaugh, A.R.; Klie, R.F.; Zhu, Y.; Welch, D.O.; Suenaga, M. Oxidation state and lattice expansion of CeO_{2-x} nanoparticles as a function of particle size. *Phys. Rev. B* **2004**, *69*, 125415. [CrossRef]
81. Fuentes, R.O.; Acuña, L.M.; Albornoz, C.A.; Leyva, A.G.; Sousa, N.; Figueiredo, F.M. Structural, physical and chemical properties of nanostructured nickel-substituted ceria oxides under reducing and oxidizing conditions. *RSC Adv.* **2016**, *6*, 64861–64870. [CrossRef]
82. Wrobel, G.; Sohler, M.P.; D’Huysser, A.; Bonnelle, J.P.; Marcq, J.P. Hydrogenation catalysts based on nickel and rare earth oxides. Part II: XRD, electron microscopy and XPS studies of the cerium-nickel-oxygen-hydrogen system. *Appl. Catal. A Gen.* **1993**, *101*, 73–93. [CrossRef]
83. Zhang, J.; Ke, C.; Wu, H.; Yu, J.; Wang, J.; Wang, Y. Solubility limits, crystal structure and lattice thermal expansion of Ln₂O₃ (Ln = Sm, Eu, Gd) doped CeO₂. *J. Alloys Compd.* **2017**, *718*, 85–91. [CrossRef]

84. Gong, W.; Zhang, R.; Chen, Z. Thermodynamic modelling and applications of Ce–La–O phase diagram. *Trans. Nonferrous Met. Soc. China* **2011**, *21*, 2671–2676. [CrossRef]
85. Wilkes, M. Catalytic studies on ceria lanthana solid solutions III. Surface segregation and solid state studies. *J. Catal.* **2003**, *219*, 305–309. [CrossRef]
86. Chen, M.; Zheng, H.; Shi, C.; Zhou, R.; Zheng, X. Synthesis of nanoparticle Ce–Mg–O mixed oxide as efficient support for methane oxidation. *J. Mol. Catal. A Chem.* **2005**, *237*, 132–136. [CrossRef]
87. Nguyen, V.-K.; Park, J.-H.; Shin, C.-H. Synthesis, characterization and catalytic performance of binary CeO₂–MgO oxides in the dehydrogenation of ethylbenzene. *React. Kinet. Mech. Catal.* **2012**, *107*, 157–165. [CrossRef]
88. Dimitrov, M.D.; Ivanova, R.N.; Stengl, V.; Henych, J.; Kovacheva, D.G.; Tsoncheva, T.S. Optimization of CeO₂–ZrO₂ mixed oxide catalysts for ethyl acetate combustion. *Bulg. Chem. Commun.* **2015**, *47*, 323–329.
89. Martínez-Arias, A.; Fernández-García, M.; Salamanca, L.N.; Valenzuela, R.X.; Conesa, J.C.; Soria, J. Structural and Redox Properties of Ceria in Alumina-Supported Ceria Catalyst Supports. *J. Phys. Chem. B* **2000**, *104*, 4038–4046. [CrossRef]
90. Weber, W.H.; Hass, K.C.; McBride, J.R. Raman study of CeO₂: Second-order scattering, lattice dynamics, and particle-size effects. *Phys. Rev. B* **1993**, *48*, 178–185. [CrossRef]
91. Sánchez-Escribano, V.; Fernández López, E.; Panizza, M.; Resini, C.; Gallardo Amores, J.M.; Busca, G. Characterization of cubic ceria–zirconia powders by X-ray diffraction and vibrational and electronic spectroscopy. *Solid State Sci.* **2003**, *5*, 1369–1376. [CrossRef]
92. Yao, X.; Tang, C.; Ji, Z.; Dai, Y.; Cao, Y.; Gao, F.; Dong, L.; Chen, Y. Investigation of the physicochemical properties and catalytic activities of Ce_{0.67}M_{0.33}O₂ (M = Zr⁴⁺, Ti⁴⁺, Sn⁴⁺) solid solutions for NO removal by CO. *Catal. Sci. Technol.* **2013**, *3*, 688–698. [CrossRef]
93. Li, L.; Chen, F.; Lu, J.-Q.; Luo, M.-F. Study of Defect Sites in Ce_{1-x}M_xO_{2-δ} (x = 0.2) Solid Solutions Using Raman Spectroscopy. *J. Phys. Chem. A* **2011**, *115*, 7972–7977. [CrossRef]
94. Guo, M.; Lu, J.; Wu, Y.; Wang, Y.; Luo, M. UV and visible Raman studies of oxygen vacancies in rare-earth-doped ceria. *Langmuir* **2011**, *27*, 3872–3877. [CrossRef] [PubMed]
95. Avram, D.; Sanchez-Dominguez, M.; Cojocar, B.; Florea, M.; Parvulescu, V.; Tiseanu, C. Toward a Unified Description of Luminescence–Local Structure Correlation in Ln Doped CeO₂ Nanoparticles: Roles of Ln Ionic Radius, Ln Concentration, and Oxygen Vacancies. *J. Phys. Chem. C* **2015**, *119*, 16303–16313. [CrossRef]
96. Al-Fatesh, A.S.A.; Fakeeha, A.H. Effects of calcination and activation temperature on dry reforming catalysts. *J. Saudi Chem. Soc.* **2012**, *16*, 55–61. [CrossRef]
97. Braid, N.; Bastien, S.; Blanchard, J.; Fauteux-Lefebvre, C.; Achouri, I.E.; Abatzoglou, N. Activation mechanism and microstructural evolution of a YSZ/Ni-alumina catalyst for dry reforming of methane. *Catal. Today* **2017**, *291*, 99–105. [CrossRef]
98. Shan, W.; Luo, M.; Ying, P.; Shen, W.; Li, C. Reduction property and catalytic activity of Ce_{1-x}Ni_xO₂ mixed oxide catalysts for CH₄ oxidation. *Appl. Catal. A Gen.* **2003**, *246*, 1–9. [CrossRef]
99. Lamonier, C.; Ponchel, A.; D’Huysser, A.; Jalowiecki-Duhamel, L. Studies of the cerium-metal-oxygen-hydrogen system (metal = Cu, Ni). *Catal. Today* **1999**, *50*, 247–259. [CrossRef]
100. Jalowiecki-Duhamel, L.; Zarrour, H.; D’Huysser, A. Hydrogen production at low temperature from methane on cerium and nickel based mixed oxides. *Int. J. Hydrogen Energy* **2008**, *33*, 5527–5534. [CrossRef]
101. Fang, W.; Pirez, C.; Paul, S.; Capron, M.; Jobic, H.; Dumeignil, F.; Jalowiecki-Duhamel, L. Room Temperature Hydrogen Production from Ethanol over CeNi_xH_zO_y Nano-Oxyhydride Catalysts. *ChemCatChem* **2013**, *5*, 2207–2216. [CrossRef]
102. Wang, Y.H.; Liu, H.M.; Xu, B.Q. Durable Ni/MgO catalysts for CO₂ reforming of methane: Activity and metal-support interaction. *J. Mol. Catal. A Chem.* **2009**, *299*, 44–52. [CrossRef]
103. Natesakhawat, S.; Oktar, O.; Ozkan, U.S. Effect of lanthanide promotion on catalytic performance of sol-gel Ni/Al₂O₃ catalysts in steam reforming of propane. *J. Mol. Catal. A Chem.* **2005**, *241*, 133–146. [CrossRef]
104. Cao, P.; Tang, P.; Bekheet, M.F.; Du, H.; Yang, L.; Haug, L.; Gili, A.; Bischoff, B.; Gurlo, A.; Kunz, M.; et al. Atomic-Scale Insights into Nickel Exsolution on LaNiO₃ Catalysts via In Situ Electron Microscopy. *J. Phys. Chem. C* **2022**, *126*, 786–796. [CrossRef]
105. Marinho, A.L.A.; Rabelo-Neto, R.C.; Epron, F.; Bion, N.; Toniolo, F.S.; Noronha, F.B. Embedded Ni nanoparticles in CeZrO₂ as stable catalyst for dry reforming of methane. *Appl. Catal. B Environ.* **2020**, *268*, 118387. [CrossRef]
106. Pinto, F.M.; Suzuki, V.Y.; Silva, R.C.; La Porta, F.A. Oxygen Defects and Surface Chemistry of Reducible Oxides. *Front. Mater.* **2019**, *6*, 260. [CrossRef]
107. Klabunde, K.J.; Stark, J.; Koper, O.; Mohs, C.; Park, D.G.; Decker, S.; Jiang, Y.; Lagadic, I.; Zhang, D. Nanocrystals as stoichiometric reagents with unique surface chemistry. New adsorbents for air purification. *Nanostructured Mater.* **1999**, *12*, 463–466. [CrossRef]
108. Ismagilov, Z.R.; Matus, E.V.; Li, L. Catalytic methods of converting carbon dioxide into useful products to reduce the impact of coal generation on global climate change. *Uspekhi Fiz. Nauk.* **2022**, *192*, 1214–1230. [CrossRef]
109. Roh, H.S.; Koo, K.Y.; Yoon, W.L. Combined reforming of methane over co-precipitated Ni–CeO₂, Ni–ZrO₂ and Ni–Ce_{0.8}Zr_{0.2}O₂ catalysts to produce synthesis gas for gas to liquid (GTL) process. *Catal. Today* **2009**, *146*, 71–75. [CrossRef]
110. Li, P.; Park, Y.H.; Moon, D.J.; Park, N.C.; Kim, Y.C. Carbon deposition onto Ni-Based catalysts for combined steam/CO₂ reforming of methane. *J. Nanosci. Nanotechnol.* **2016**, *16*, 1562–1566. [CrossRef]
111. Siang, T.J.; Pham, T.L.; Van Cuong, N.; Phuong, P.T.; Phuc, N.H.H.; Truong, Q.D.; Vo, D.V.N. Combined steam and CO₂ reforming of methane for syngas production over carbon-resistant boron-promoted Ni/SBA-15 catalysts. *Microporous Mesoporous Mater.* **2018**, *262*, 122–132. [CrossRef]

112. Wysocka, I.; Mielewczyk-Gryń, A.; Łapiński, M.; Cieślik, B.; Rogala, A. Effect of small quantities of potassium promoter and steam on the catalytic properties of nickel catalysts in dry/combined methane reforming. *Int. J. Hydrogen Energy* **2021**, *46*, 3847–3864. [[CrossRef](#)]
113. Sukonket, T.; Khan, A.; Saha, B.; Ibrahim, H.; Tantayanon, S.; Kumar, P.; Idem, R. Influence of the Catalyst Preparation Method, Surfactant Amount, and Steam on CO₂ Reforming of CH₄ over 5Ni/Ce_{0.6}Zr_{0.4}O₂ Catalysts. *Energy Fuels* **2011**, *25*, 864–877. [[CrossRef](#)]
114. Zhao, Z.; Ren, P.; Li, W.; Miao, B. Effect of mineralizers for preparing ZrO₂ support on the supported Ni catalyst for steam-CO₂ bi-reforming of methane. *Int. J. Hydrogen Energy* **2017**, *42*, 6598–6609. [[CrossRef](#)]
115. Agarwal, S.; Mojet, B.L.; Lefferts, L.; Datye, A.K. Ceria Nanoshapes—Structural and Catalytic Properties. In *Catalysis by Materials with Well-Defined Structures*; Elsevier: Amsterdam, The Netherlands, 2015; pp. 31–70. [[CrossRef](#)]
116. Dai, Y.; Lu, P.; Cao, Z.; Campbell, C.T.; Xia, Y. The physical chemistry and materials science behind sinter-resistant catalysts. *Chem. Soc. Rev.* **2018**, *47*, 4314–4331. [[CrossRef](#)] [[PubMed](#)]
117. Gonzalez-DelaCruz, V.M.; Holgado, J.P.; Pereñíguez, R.; Caballero, A. Morphology changes induced by strong metal-support interaction on a Ni-ceria catalytic system. *J. Catal.* **2008**, *257*, 307–314. [[CrossRef](#)]
118. Rehman, S.; Kim, H.; Farooq Khan, M.; Hur, J.H.; Lee, A.D.; Kim, D.K. Tuning of ionic mobility to improve the resistive switching behavior of Zn-doped CeO₂. *Sci. Rep.* **2019**, *9*, 193870. [[CrossRef](#)]
119. Ismagilov, I.Z.; Matus, E.V.; Nefedova, D.V.; Kuznetsov, V.V.; Yashnik, S.A.; Kerzhentsev, M.A.; Ismagilov, Z.R. Effect of support modification on the physicochemical properties of a NiPd/Al₂O₃ catalyst for the autothermal reforming of methane. *Kinet. Catal.* **2015**, *56*, 394–402. [[CrossRef](#)]
120. Chan, S.H.; Wang, H.M. Effect of natural gas composition on autothermal fuel reforming products. *Fuel Process. Technol.* **2000**, *64*, 221–239. [[CrossRef](#)]
121. Zhu, J.; Zhang, D.; King, K.D. Reforming of CH₄ by partial oxidation: Thermodynamic and kinetic analyses. *Fuel* **2001**, *80*, 899–905. [[CrossRef](#)]